

Chapter 12

KPFM and PFM of Biological Systems

B.J. Rodriguez and S.V. Kalinin

Abstract Surface potentials and electrostatic interactions in biological systems are key elements of cellular regulation and interaction. Examples include cardiac and muscular activity, voltage-gated ion channels, protein folding and assembly, and electroactive cells and electrotransduction. The coupling between electrical, mechanical, and chemical signals and responses in cellular systems necessitates the development of tools capable of measuring the distribution of charged species, surface potentials, and mechanical responses to applied electrical stimuli and vice versa, ultimately under physiological conditions. In this chapter, applications of voltage-modulated atomic force microscopy (AFM) methods including Kelvin probe force microscopy (KPFM) and piezoresponse force microscopy (PFM) to biological systems are discussed. KPFM is a force-sensitive non-contact or intermittent-contact mode AFM technique that allows electrostatic interactions and surface potentials to be addressed. Beyond long-range electrostatic interactions, the application of bias can lead to a mechanical response, e.g., due to linear piezoelectric coupling in polar biopolymers or via more complex electrotransduction and redox pathways in other biosystems. The use and development of PFM, based on direct electromechanical detection, to biological systems will also be addressed. The similarities and limitations of measuring surface potentials and electromechanical coupling in solution will be outlined.

B.J. Rodriguez (✉)

Conway Institute of Biomolecular and Biomedical Research, University College Dublin, Belfield, Dublin 4, Ireland

e-mail: brian.rodriquez@ucd.ie

S.V. Kalinin

Materials Science and Technology Division and Center for Nanophase Materials Science, Oak Ridge National Laboratory, Oak Ridge, TN 37831, USA

e-mail: brian.rodriquez@ucd.ie

12.1 Introduction

12.1.1 *Electric Potentials and Electromechanics in Biosystems*

Electrostatic interactions and electromechanical coupling in biological systems are key to biological structure and functionality, and span length scales from the single molecule to the cellular level and beyond [1–6]. The most widely known examples include muscle contraction, hearing, and voltage-gated ion channels. The electrostatics of proteins, membranes, and their interactions with each other and their environment have been broadly studied [7–13]. It is thought that charged surface residues impact protein folding and stability [14], and that long-range electrostatic forces drive initial nonspecific protein-protein associations [15]. The surface potential of cellular membranes varies according to the lipid composition, and the negative surface charge on the inner plasma membrane plays a role in cellular signaling to initiate, e.g., phagosome formation [16, 17]. The electric potential differences across a membrane regulate the proton transfer process of proton pumps [18, 19]. Electric fields associated with membranes often extend beyond the associated membrane deep into the cytosol as was recently shown for mitochondrial membranes [20], and models have been proposed which describe a three dimensional electric field cellular signaling network with the nucleus at the center of a cytoskeletal network [21]. Membrane surface charges also influence the formation of calcium microdomains [22], place constraints on protein anchoring [23] and import [24], and regulate membrane protein function, including electroconformational coupling [25–27] and the gating of ion channel proteins [28–30]. The complexity of the electrostatic interactions on a single membrane level can be illustrated in Fig. 12.1a. Note that the presence of the proteins in the membrane will affect local charge distributions making the membrane potential laterally inhomogeneous. In addition, deformation of the membrane will change potential distributions due to the flexoelectric effect.

These electrostatic interactions are fundamental to biological processes at the molecular and cellular levels, and the improper generation or sensing of electric signals can indicate significant deviations in biological function. Recently, it was shown that a reduction in the neuronal membrane potential is associated with Alzheimer's [32]. Similarly, membrane potentials are tied to cell cycle and death [33]. Beneficial and detrimental effects of external fields on tissue formation and repair have been studied in detail [34, 35].

Clearly, electric fields and electrostatic interactions are an integral component of the complete biophysical picture. These electrical signals are strongly linked to mechanical responses, e.g., as a conformational change in a protein or cellular electrotransduction and the mechanisms by which a cell converts an electrical signal to a chemical or mechanical response. Similarly, mechanical stimuli can result in an electrical signal. This class of interactions are described as electromechanical coupling and can take multiple forms, ranging from relatively simple mechanisms such as membrane flexoelectricity and biopolymer piezoelectricity [36, 37] to auditory

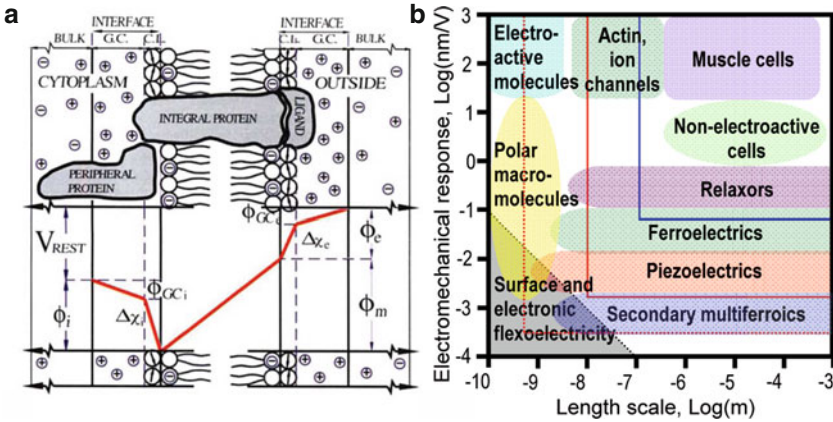


Fig. 12.1 (a) Electrostatics across a cellular plasma membrane. At each membrane interface, the negative charge of the polar heads of the phospholipids is compensated by a cationic Gouy–Chapman (GC) layer separated by a compact layer (CL) of strongly polarized water molecules. Electric potential (ϕ) is the sum of the potential across the CL ($\Delta\chi$) and the GC (ϕ_{GC}). (b) Electromechanical coupling in functional materials. The solid blue and red lines correspond to estimated limits of nanoindentation and atomic force microscopy, respectively, while the dashed red lines correspond to the ultimate limits that can be achieved through the instrumentation development including resonant-enhanced modes, low-noise beam deflection position systems, and high-stability platforms. Panel (a) reproduced with permission from [6]. Copyright 1996, John Wiley & Sons, Inc. Panel (b) adapted with permission from [31]. Copyright 2008, Elsevier

and sensory activity that amplifies high-frequency signals [5]. Note that in biological systems, the traditional separation of electromechanical interactions into long-range electrostatic forces and electromechanical piezoelectric and electrostrictive interactions is challenging. For example, the presence of mobile ions will render electrostatic interactions short-ranged and screened at the scale of the corresponding Debye length. Furthermore, the interplay between ionic field motion and specific adsorption gives rise to a broad range of electrocapillary phenomena that can be interpreted differently dependent on the scale of the observation (e.g., local electrostatic interactions and tissue-level piezoelectric coupling). Correspondingly, we aim to keep the discussion general to include all forms of electromechanical coupling in biosystems.

Typical values of electromechanical response for a wide range of functional materials and systems are shown in Fig. 12.1b. Piezoelectricity is the linear coupling in a material between a mechanical strain and an electric polarization (or a redistribution of charge), or, conversely, between an applied field and a mechanical deformation, both more generally referred to as electromechanical coupling, and has been observed in calcified tissues such as bone. This has prompted speculation that piezoelectricity could be partially responsible for biomineralization (the formation and mineralization of bone and dental tissues) and bone remodeling (the process of bone tissue renewal, which depends on the regulation of osteoclast and osteoblast

activity). In fact, a key missing element of understanding mechanotransduction in bone cell regulation is how bone cells sense mechanical stimuli of different magnitudes, direction, and duration [38]. Wolff's law [39] states that bone develops and adapts (self-organizes) to mechanical stresses to produce a structure best-suited to withstand the applied stress. Thus, the direction-dependent piezoelectricity of collagen, which generates an electric potential proportional to an applied stress, is an intriguing mechanism by which osteoclast and osteoblast cells can sense where bone should be resorbed or formed, respectively.

This relation between mechanics and change in potential underscores the importance of being able to measure both electrical and electromechanical interactions in biological systems. The coupling between electrical, mechanical, and chemical signals and responses in molecular and cellular systems necessitates the development of tools capable of measuring the distribution of charged species, surface potentials, and mechanical responses to applied electrical stimuli and vice versa, ultimately under physiological conditions. Atomic force microscopy (AFM) [40] is ideally suited to measure electrostatic and electromechanical interactions owing to the high lateral and force resolution it offers. Below, we discuss the implementation of two complementary voltage-modulated AFM methods, namely, Kelvin probe force microscopy (KPFM) as a method to study electrostatic interactions and piezoresponse force microscopy (PFM) as a method to study electromechanical coupling in biosystems. We emphasize that while for low-resolution ambient and ultra-high vacuum imaging, these techniques can be clearly differentiated (noncontact and contact regimes, respectively), for high-resolution studies achieving molecular and atomic resolution [41] and for studies in liquid environments (no jump-to-contact instability), this separation is somewhat artificial, and both electrostatic and electromechanical interactions must be taken into account to give a full picture of voltage-induced mechanical responses as deduced from the measured signals.

12.1.2 Voltage Modulation SPM for Electrical and Electromechanical Measurements

12.1.2.1 Kelvin Probe Force Microscopy

In this section, the use of electrostatic force microscopy (EFM) and KPFM to measure electric fields and contact potential differences are briefly discussed. These intermittent or noncontact voltage-modulated AFM techniques are widely used scanning probe microscopy (SPM)-based techniques for the determination of electric interactions and electronic structure, including surface potentials, band bending, and surface state densities, especially in inorganic and organic semiconductors and often in ultra-high vacuum. Detailed descriptions of EFM [42, 43] and KPFM [44–46] can be found elsewhere, including this book.

There are several approaches to implementing EFM and KPFM. Often these techniques utilize an approach developed by Terris et al. [42] and Saurenbach et al. [43] which uses a mechanically driven cantilever and a voltage modulation applied to the tip, allowing topographic and electrostatic images to be acquired simultaneously, or in sequential line scans using a lift-height or interleave approach. The key distinctions between the techniques are that in EFM, generally the electrostatic and capacitive forces on the tip are measured as the changes in the dynamic response of a mechanically driven, electrically biased cantilever. In KPFM, the cantilever is driven by periodic ac bias, and a feedback loop is used which minimizes the amplitude of the force on the cantilever (amplitude modulation KPFM) or the force gradient (frequency modulation KPFM [47–49]). In KPFM, the electric potential on the conductive SPM probe is modulated as $V_{\text{tip}} = V_{\text{dc}} + V_{\text{ac}}\cos(\omega t)$, where V_{dc} is the static potential offset, V_{ac} is the driving voltage, and the driving frequency ω is typically chosen close to the free cantilever resonance. The tip bias results in the capacitive tip–surface force, $F_{\text{el}} = C'_z(V_{\text{tip}} - V_s - \Delta\text{CPD})^2$, where C'_z is the (unknown) tip–surface capacitance gradient, V_s is the electrostatic surface potential, and ΔCPD is the contact potential difference between the tip and the surface. Depending on the experimental configuration, the voltage modulation can be applied either during the interleave scan (i.e., when the tip retraces the predetermined surface topography while maintaining constant tip–surface separation), or during the acquisition of topographic information (at a different frequency). A lock-in amplifier is used to select the first harmonic component of the electrostatic force on the tip, $F_{\text{el}}(1\omega) = C'_z V_{\text{ac}}(V_{\text{dc}} - V_s - \Delta\text{CPD})$. In KPFM, a feedback loop is engaged to keep this component zero by adjusting the static offset of the tip potential, V_{dc} . The condition $F_{\text{el}}(1\omega) = 0$ is satisfied when $V_{\text{dc}} = V_s + \Delta\text{CPD}$, i.e., when the microscope-controlled compensation potential is equal to the (unknown) local surface potential. On a (nominally) grounded surface, KPFM allows direct detection of the materials-specific contact potential, containing the contributions from surface dipole layers, non-equilibrium surface charges, etc. The theory of spatial resolution, the effect of topographic inhomogeneities (topographic cross-talk), and the image formation mechanism in KPFM for conductive and semiconductive materials have been studied extensively [50]. The resulting images are of the combined electric and capacitive force on the probe and cantilever in the case of EFM, and the bias which minimizes these forces or force gradients in the case of KPFM. This bias is related to the contact potential difference between the tip material or coating and the sample and the electronic structure of the sample. In solution, this can further be related to the isoelectric point. A schematic for interleave-mode KPFM is shown in Fig. 12.2a. Note that the KPFM signal is controlled by the tip–surface force acting across the tip-sample gap and does not depend on the field inside the material (Fig. 12.2c). Furthermore, for most materials, the mismatch between the dielectric constants of the imaging environment and the material implies that the potential drops significantly in the tip–surface gap. In intermittent-contact KPFM, both electrostatic and electromechanical to the signal contributions are present.

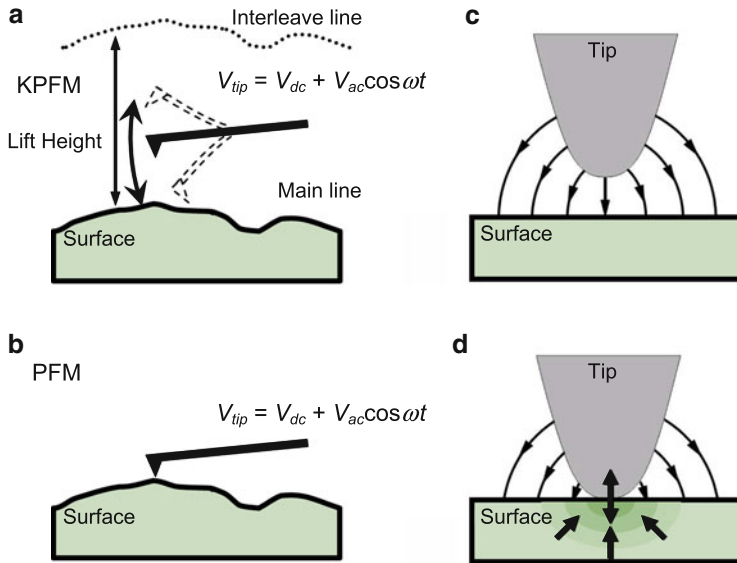


Fig. 12.2 Schematics showing (a,c) KPFM and (b,d) PFM imaging principles. (c) In KPFM, electrostatic forces act on the tip in the tip–surface gap. (d) In PFM, electrostatic and electromechanical (double arrow) forces are present. Strain is indicated in (d). (c,d) Adapted with permission from [51]. Copyright 2006, American Physical Society

12.1.2.2 Piezoresponse Force Microscopy

Piezoresponse force microscopy is a voltage-modulated contact-mode AFM technique. In PFM [52–59], an electrically conductive tip traces surface topography using standard deflection-based feedback, during which time, a sinusoidal electrical bias, $V_{\text{tip}} = V_{\text{dc}} + V_{\text{ac}}\cos(\omega t)$, is applied to the tip. The electromechanical response of the surface, e.g., the local piezoelectrically induced mechanical deformation of the sample due to the applied field, is detected as the first harmonic component of the bias-induced tip deflection, $d_{1\omega}\cos(\omega t + \varphi)$, as shown in Fig. 12.2b. The response amplitude, $d_{1\omega}$, is a measure of the local electromechanical activity of the surface, while the phase of the piezoresponse, φ , provides information on the polarization direction or polar orientation below the tip. In the case of ferroelectric materials, for c^- domains (polarization vector pointing downward) the application of a positive tip bias results in the expansion of the sample and surface oscillations are in phase with the tip voltage, $\varphi = 0$. For c^+ domains, $\varphi = 180^\circ$. In the case of piezoelectric biomaterials, the phase is coupled to polar orientation yielding similar phase responses. The PFM signal is usually plotted as a pair of amplitude-phase, $A = d_{1\omega}/V_{\text{ac}}$, φ , images, or as a mixed piezoresponse (PR) signal, $\text{PR} = A\cos\varphi$. This AFM-based approach for measuring electromechanical response was first

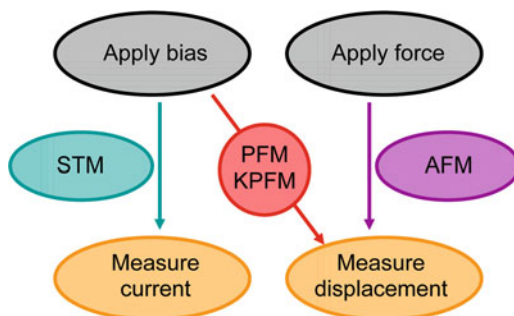
demonstrated by Günther and Dransfeld on thin copolymer films of polyvinylidene fluoride and trifluoroethylene [60].

Both flexural and torsional components of tip displacement can be probed, giving rise to out-of-plane (vertical) and in-plane (lateral) PFM (VPFM and LPFM, respectively). By combining VPFM data with (ideally two orthogonal) LPFM data sets, the data can be represented in a vector form [61], enabling an approach for determining the three-dimensional direction of polarization in, e.g., thin films [62], crystals [63], and ferroelectric capacitors [64].

Note that the operation of PFM is complementary to that of conventional SPMs as shown in Fig. 12.3. For scanning tunneling microscopy (STM), an electrical bias is applied to a metal tip, and the tunneling current is measured, while in the case of AFM, a force is applied, and the resulting tip-deflection is measured. In PFM, an electrical bias is applied to a tip, and the tip deflection resulting from the deformation of the sample surface due to the bias-induced strain is detected. Notably, the surface deformation is dependent only on the potential drop in the material, and is not affected by the tip size. Hence, while both PFM and KPFM use a modulated voltage applied to a conducting cantilevered tip, in one case the mechanical response of material to the applied bias is measured, while in the other, the electric forces are measured or minimized to gain insight into the electronic structure. In principle, both mechanisms can operate at the same time; however, in contact mode where the tip-sample stiffness is high, bias-induced strains dominate, while in noncontact mode, electrostatic forces dominate since the tip-sample stiffness is small. As an example, KPFM can be used on conductive surfaces whereas PFM cannot. Clearly there is the possibility of an overlap, as the applied bias can lead to a mechanical deformation in the case of piezoelectric materials, and electromechanical deformations can lead to redistribution of charge and changes in surface potentials. However, these second-order effects are usually small.

In an ambient environment, the tip interacts with the surface through electrostatic forces and short-range electromechanical interactions and the piezoresponse (PR) signal can be written as a combination of the two interactions,

Fig. 12.3 Classification of SPM techniques based on the type of stimulus and response. In PFM and KPFM, a bias is applied to the AFM tip and displacements resulting from electromechanical and electric forces are measured. Adapted with permission from [36]. Copyright 2007, Annual Reviews



$PR = PR_{em} + PR_{el}$ [51]. In the low-frequency limit, the electromechanical component is

$$PR_{em} = \alpha_a(h) \tilde{d}_{33} \frac{k_1}{k_1 + k}, \quad (12.1)$$

where \tilde{d}_{33} is the effective electromechanical response of material, $\alpha_a(h)$ is the ratio of the ac tip potential to the ac surface potential of the ferroelectric (i.e., the potential drop in the tip–surface gap), k_1 is the spring constant of the tip–surface junction, and k is the spring constant of the cantilever. In ambient or vacuum, the electrostatic forces are long-range, $F_{el}^{amb} = (1/2)C'_z(z)(V_t - V_s)^2$, where V_t is the tip potential, V_s is the surface potential, and $C'_z(z)$ is the tip–surface capacitance gradient. The electrostatic contribution is

$$PR_{el}^{amb} = \left(\frac{C'_{sphere} + C'_{cone}}{k_1 + k} + \frac{C'_{cant}}{24k} \right) (V_{dc} - V_s), \quad (12.2)$$

where C'_{sphere} , C'_{cone} , and C'_{cant} are the capacitance gradients due to the spherical and conical parts of the tip and cantilever, respectively. V_{dc} is the dc potential offset of the tip bias, and h is the tip–surface separation. In a sphere-plane model for small separations, $C'_{sphere}(h) = \pi\epsilon_0 R/h$, where R is the tip radius of curvature. In ambient, $\alpha_a(h) = 1$ for $h < 0$ (contact), i.e., the response is independent of the penetration depth [65], and $\alpha_a(h) \ll 1$ for $h > 0$ (non-contact). The numerical values of coefficients in (12.2) depend on the mode of cantilever oscillations.

As discussed above, the implementation of both PFM and KPFM relies on the application of a bias to measure electromechanical coupling and electrostatic interactions, respectively. In the case of PFM, the applied ac bias leads to a surface deformation which is detected by the AFM cantilever. In KPFM, the applied ac bias allows electrostatic forces to be measured and minimized through the additional application of a dc offset. The image formation mechanisms are the effects of the combined electric, capacitive, and electromechanical forces on the probe and cantilever in the case of KPFM and PFM, with long-range forces dominating the signal for KPFM, whereas short-range forces dominate for contact-mode PFM. An example of simultaneously acquired PFM and KPFM of model ferroelectric systems are shown in Fig. 12.4 [66]. Note that in ambient, PFM yields higher resolution than KPFM since it measures strong contact forces and not long-range electrostatic forces. Often, PFM and KPFM contrast can be related (e.g., for ferroelectric domain structures [Fig. 12.4]); however, in other cases they can differ significantly.

12.2 KPFM of Biosystems

In this section, the measurements of electrostatic interactions in biological systems are explored. The applications of KPFM to measure surface potentials at the single molecular to the assembled lipid bilayer and protein membrane level are discussed.

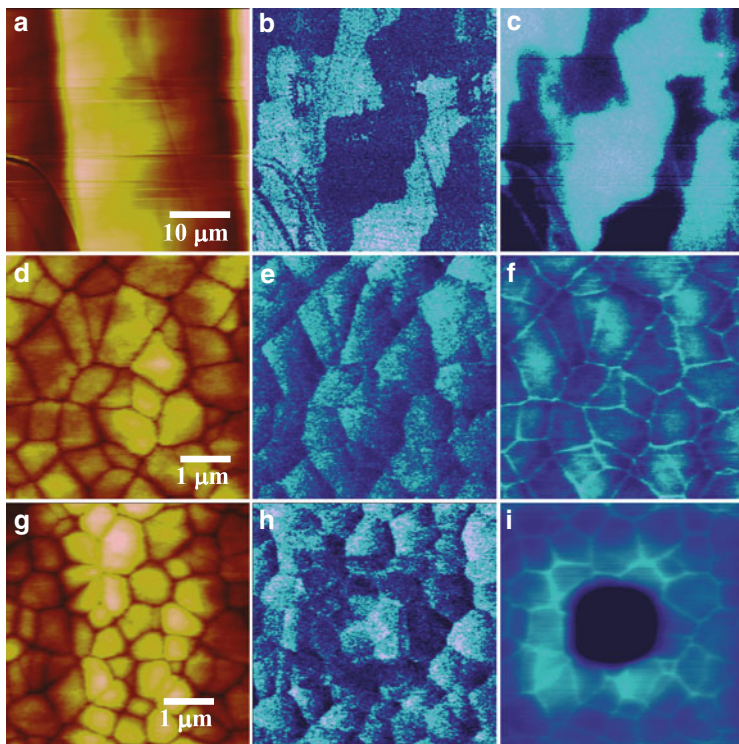


Fig. 12.4 (a,d,g) Surface topography, (b,e,h) piezoresponse, and (c,f,i) KPFM images of a BaTiO₃ (100) crystal surface (a–c) and Pb(ZrTi)O₃ film (d–i), respectively. Panels g–i have been acquired after the application of 10 V during a $2.5 \times 2.5 \mu\text{m}^2$ scan and -10 V during a $1 \times 1 \mu\text{m}^2$ scan. Reproduced with permission from [66]. Copyright 2002, American Physical Society

12.2.1 Organic Molecules

Surface potential measurements have been performed on a variety of molecular surfaces including self-assembled monolayers [67–72], Langmuir–Blodgett films [73–77], organic ferroelectric oligomers [78], and organic nanostructures [79, 80]. KPFM has been used extensively to measure electronic structure of organic molecules films and structures, and thorough reviews can be found in [81, 82] and in Chap. 11 of this book.

12.2.2 Biomolecular Systems

As discussed in Sect. 12.1, charge and surface potentials play an active role in both biological structure and function. The measurement of these interactions in cellular

biology has been primarily membrane-based, using voltage-sensitive dyes, and fluorescence and patch/voltage clamp techniques [83–89]. Recently, encapsulated voltage dyes have been used to map the electric field within a cell [20], and voltage/patch clamp techniques have been extended to subcellular structures with a smart patch-clamp system [90]. For proteins, scanning Kelvin probe [91–93] and nanoprobe [94–97] have been used by several groups to measure surface potentials of dispersed proteins and microarrays on scales ranging from ~ 1 cm to 100s of nm. In order to extend this technique to the nanoscale, as a precondition to resolve single molecules and charged groups within molecules or charged domains in membranes, a nanoscale local probe is required. An early attempt at measuring electrostatics in biosystems with an etched tungsten wire tip was made by Leng and Williams [99]. In this section, the uses of KPFM to measure biomolecular surface potentials in static and dynamic systems are discussed.

12.2.2.1 KPFM of Static Systems

Several attempts have been made to image electrostatic interactions and surface potential of biosystems using SPM (see [98] for a review). The charged backbone and necessity of fast sequencing has made DNA a popular target of KPFM measurements. Gil et al. deposited gold electrodes on DNA-coated mica and used KPFM to investigate the conductivity of DNA [100]. By applying bias to the electrodes, and measuring KPFM of DNA connected to an electrode it was determined that λ -DNA is not conductive.

Kwak et al. used a molecular combing method based on silane-modified Si substrates and the hydrodynamic force of a receding meniscus (i.e., self-orientation effect when the substrate is removed from solution) to prepare stretched single DNA molecules for KPFM measurements [101]. The contact potential difference of the sample was measured against a chemically hexadecanethiol-modified conducting AFM tip. The topography of the stretched DNA is shown in Fig. 12.5a. In Figs.

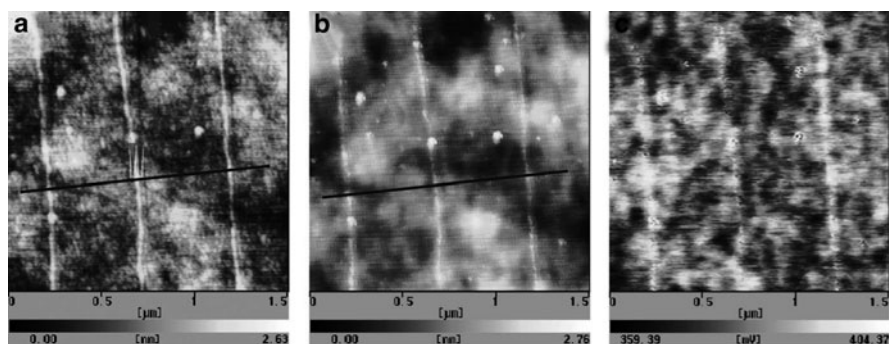


Fig. 12.5 (a) Topographic image and simultaneously obtained (b) topographic and (c) KPFM images. Reproduced with permission from [101]. Copyright 2003, Elsevier

12.5b and c, the simultaneously measured topography and KPFM images of the same region are shown. All images were measured at 48.9% relative humidity. Variations in Fig. 12.5c can be due to the mixed monolayer of NH_2^- and $\text{CH}_2=\text{CH}$ -terminated silanes. The stretched DNA strands can be seen to have a higher contact potential difference than the surrounding surface, suggesting that dipole moments formed between the surface water layer and the negatively charged DNA backbones point away from the substrate.

Mikamo-Satoh et al. reported a modified EFM study of DNA strands containing T7 RNA polymerase, which binds at a specific location on the DNA to synthesize mRNA [102]. The topography and potential images are shown in Figs. 12.6a and b, respectively. The electric potential image (Fig. 12.6b) shows dark contrast for both DNA and the polymerase transcription complex corresponding to low electric potential. Despite having different heights, the potentials for the transcription complex and tangled DNA are similar (~ -0.37 V), while the potential for isolated DNA is ~ -0.48 V as shown in the line profiles in Figs. 12.6c and d, indicating that the accumulation of DNA on the surface induces a local potential increase. Analysis of the results indicate as before an upward pointing electric dipole at the DNA due to distortion arising from a collapsed coaxial structure and partial ionization of phosphate groups with the surface water layer.

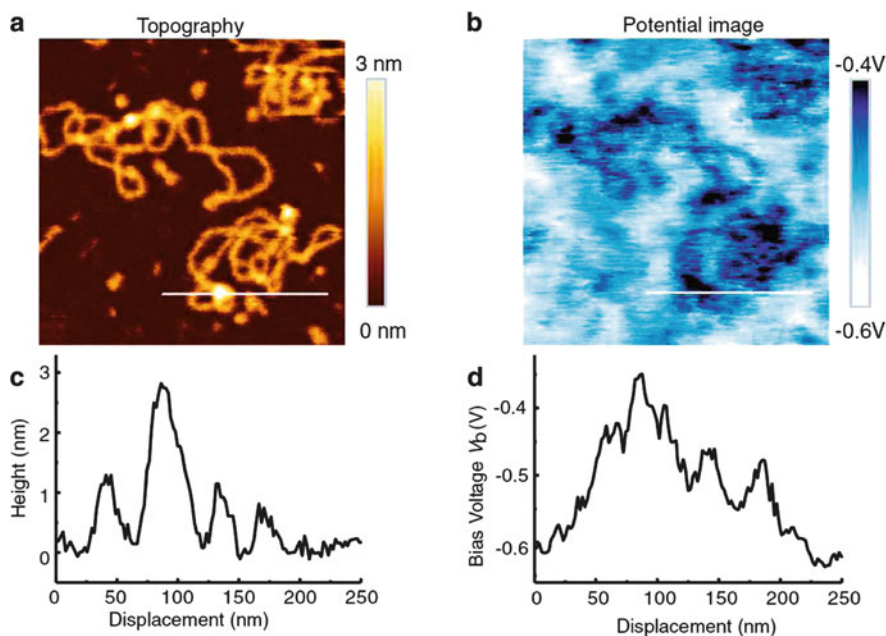


Fig. 12.6 (a) Topography and (b) electric potential images of DNA and transcription complexes of DNA. (c) Section profile of the topography showing 1.4 and 2.8 nm heights of DNA and transcription complex, respectively. (d) Section profile of the potential showing potential values of -0.45 V, -0.35 V, and -0.6 V for DNA, transcription complex, and mica, respectively. Reproduced with permission from [102]. Copyright 2009, Institute of Physics

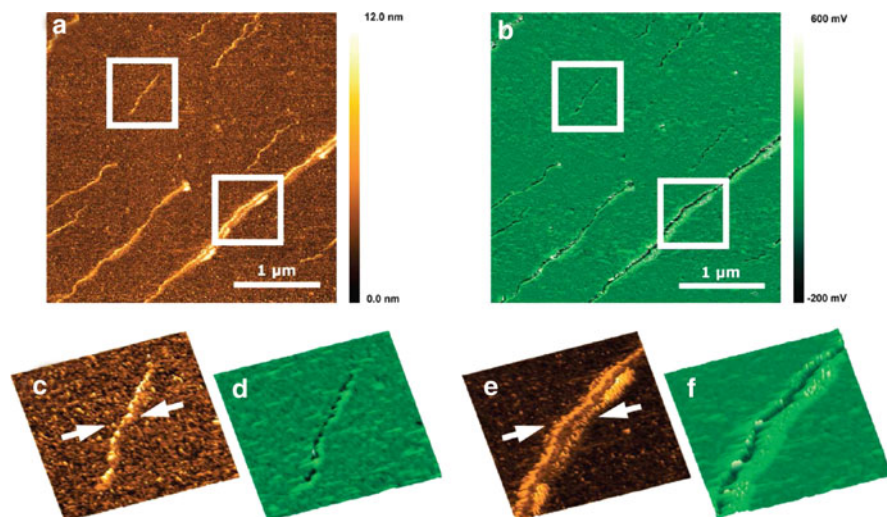


Fig. 12.7 (a) Topography image of single and multiple DNA strands on a silicon surface. (b) Corresponding KPFM scan of the same area showing a more negative potential for the DNA strands than the substrate. Regions of the (c,e) topography and (d,f) KPFM scans showing (c,d) single and (e,f) multiple DNA strands. Reproduced with permission from [103]. Copyright 2009, American Chemical Society

KPFM of DNA molecules and counterions have been reported recently by Leung et al. [103, 104] using a dual frequency mode. In Fig. 12.7a, the height image shows single and multiple DNA strands. The corresponding KPFM image (Fig. 12.7b) shows that the DNA is always at a more negative potential than the substrate. Upon closer inspection of single (Figs. 12.7c and d) and multiple (Figs. 12.7e and f) DNA strands, it is apparent that there is a slight increase in positive potential at the edges of the DNA. The authors attribute this to the presence of buffer salt deposits which have dried adjacent to the DNA. A shell of positively charged counterions gives DNA its stability. The multiple DNA strands have a more negative measured surface potential, and the associated counterions have a higher positive potential than those for a single DNA strand.

Note that KPFM of biological systems can be strongly affected by surface topography irregularities that can provide a discernible contrast even on a chemically uniform surface. An example of this topographic cross-talk on an as-deposited gold surface was reported by Efimov and Cohen [105]. Recent studies of the cross-talk effect are reported in Chap. 4. The practical consequence of the presence of cross-talk is that the cross-talk should be taken into account in the interpretation of KPFM data.

KPFM can be applied to any biomolecule which has charge or dipole moment. Another example of KPFM measurements of charged biomolecules was reported by Leung et al. [103]. In Fig. 12.8a, the topography image of avidin molecules adsorbed on silicon is shown. From the KPFM image (Fig. 12.8b) it is apparent that

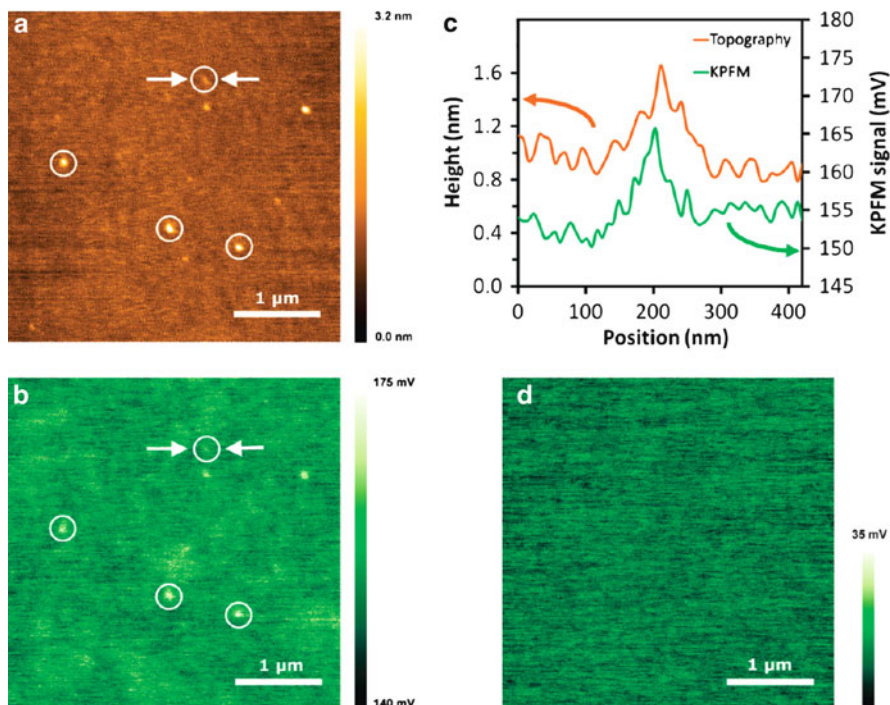


Fig. 12.8 (a) Topography and (b) KPFM images of avidin molecules (*circled*) deposited on a silicon substrate (c) Line profiles of the avidin molecule at the location indicated by arrows in (b). (d) KPFM image of a bare silicon substrate. Reproduced with permission from [103]. Copyright 2009, American Chemical Society

these avidin molecules have a positive surface potential 10–15 mV higher than the substrate. This is further illustrated via line profiles of the topography and KPFM signal across an avidin molecule (Fig. 12.8c). In the absence of avidin molecules, no such surface potential variation can be seen (Fig. 12.8d). This observation supports the attribution of the signal in Fig. 12.8b to intrinsic surface potential variations rather than cross-talk.

Another example of KPFM applied to the characterization of surface potentials of biomolecules is the study of human plasma fibrinogen deposited on highly ordered pyrolytic graphite (HOPG) presented by Ohta et al. [106] and shown in Fig. 12.9. Typical examples of topographic images of single fibrinogen molecules and fibrinogen fibrils of single molecule widths are shown in Figs. 12.9a and b, respectively. KPFM images of the surface potential of isolated or aggregated fibrinogen molecules are shown in Fig. 12.9c. In Fig. 12.9d, KPFM of fibrinogen aggregated into fibers are shown, which demonstrate a periodic surface potential dependence, indicated by arrows, corresponding to the different polypeptide domains present in fibrinogen.

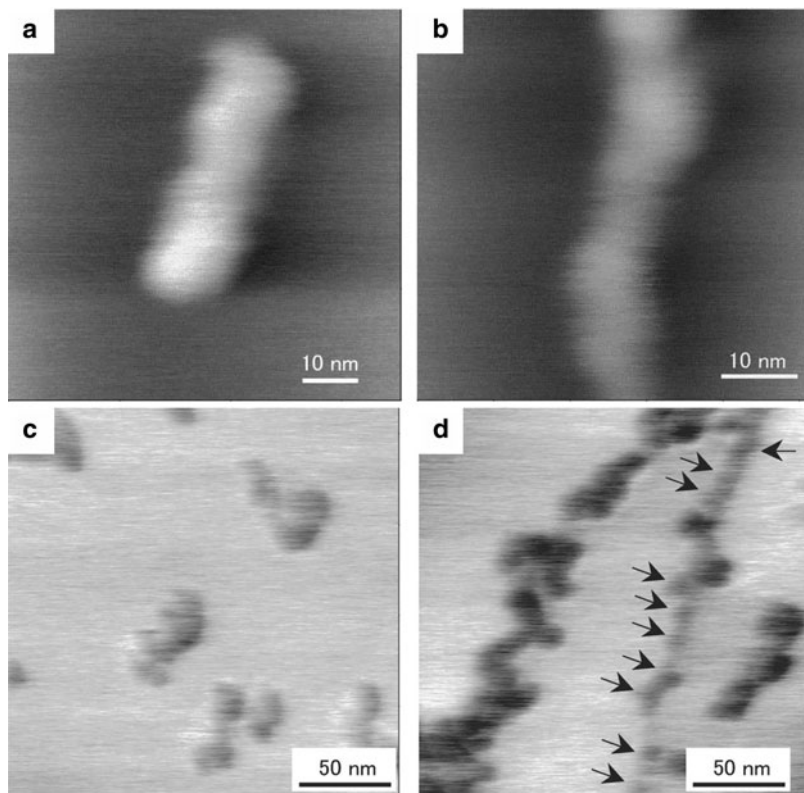


Fig. 12.9 (a,b) Topography images of a single fibrinogen molecule and a single-molecule wide fibrinogen fibril. (c) KPFM image of isolated and aggregated fibrinogen molecules adsorbed on a HOPG substrate. (d) KPFM image of fibrinogen aggregates composed of fibers. Reproduced with permission from [106]. Copyright 2006, Elsevier

The group of Gomila has made several significant contributions to electrical-based characterization of supported biomembranes using non-contact dual-pass approaches to measure dielectric constants [107, 108]. In one approach, based on nanoscale capacitance microscopy [109], the topography is measured in the first pass in a standard dynamic mode and the height is retraced in the second pass at a constant-height to measure the variation in local capacitance. The dielectric constant can then be determined from the capacitance and scan height [107]. In other words, the second harmonic of the force on the tip is a measure of the dielectric constant. In the second approach [108], standard DC EFM is used with an appropriate analytical model to determine the dielectric constant with knowledge of the applied bias, the bias-induced deflection, and the lift-height. Both approaches have been demonstrated on purple membrane fragments and the obtained values for the dielectric constant are in good agreement (Fig. 12.10).

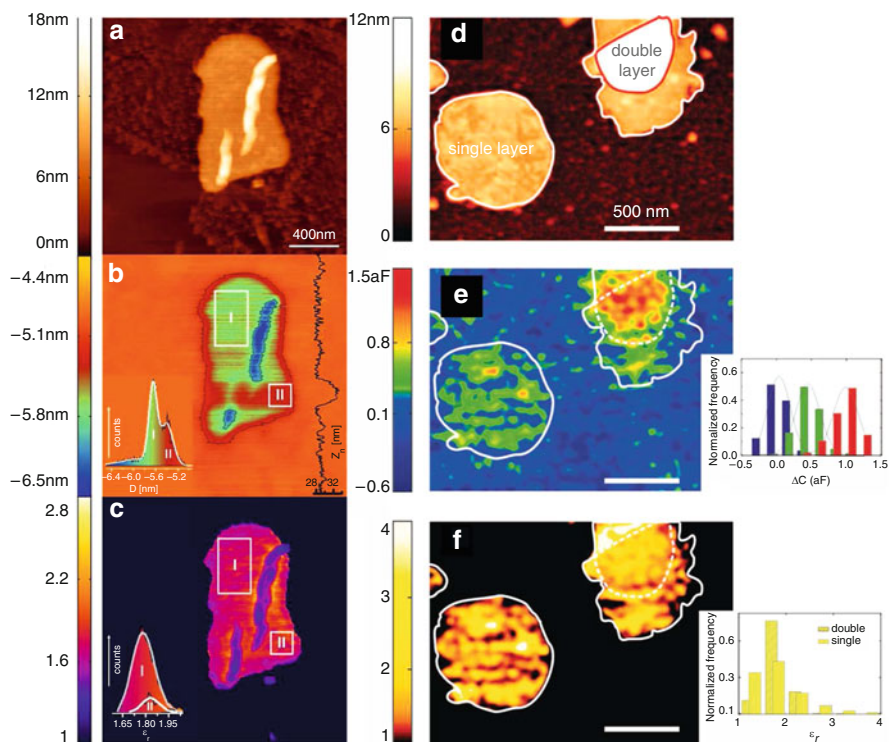


Fig. 12.10 Dielectric constant measurements on single and double layer purple membranes using (a–c) DC EFM and (d–f) nanoscale capacitance approaches. (a) Topography, (b) DC EFM cantilever deflection, and (c) the extracted dielectric constant of a single layer patch. Histograms in (b,c) show the distribution of the cantilever deflection and the dielectric constant on the purple membrane, respectively. (d) Topography, (e) local capacitance, and the extracted dielectric constant of single and double layer purple membranes. (a–c) Reproduced with permission from [108]. Copyright 2009, Institute of Physics. (d–f) Reproduced with permission from [107]. Copyright 2009, American Chemical Society

12.2.2.2 KPFM of Dynamic Chemical Phenomena

While static KPFM images measured on uneven surfaces can always contain cross-talk, observation of dynamic changes of potential that leave the topography invariant are generally much more reliable. The examples of such studies include polarization switching in ferroelectric materials [110] and photo-induced phenomena in semiconductors [49, 111, 112]. Similarly, the potential of KPFM extends beyond the imaging of static biomolecules – it can also be applied to detect changes in surface potential as a result of specific chemical or optical events, as will be discussed now. Sinensky and Belcher used a combination of dip pen lithography and KPFM to extend the Kelvin probe measurements for microassays to the nanoscale [113]. In this manner, local changes in charge densities due to the formation of specific

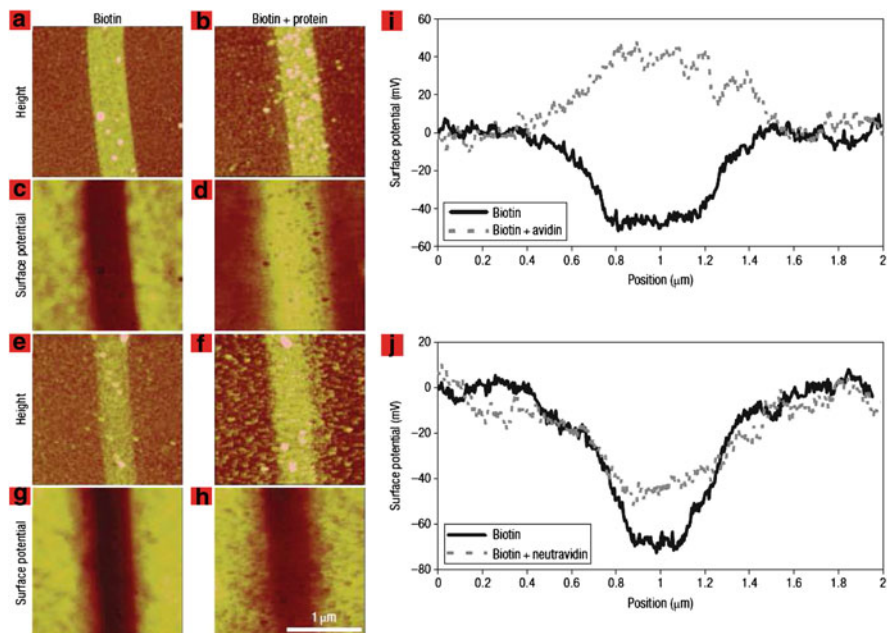


Fig. 12.11 (a–d) Topography and KPFM images of the patterned biotin sample before and after exposure to avidin. (e–h) Topographic and KPFM images of the immobilized biotin sample before and after exposure to neutravidin. (i), (j) Line profiles of the surface potential. Reproduced with permission from [113]. Copyright 2007, Nature Publishing Group

biomolecular complexes (the presence of specific bound target biomolecules) can be identified without labeling or special chemistries. They looked specifically at avidin-biotin binding and DNA probes.

The effect of binding of avidin and neutravidin with surface-immobilized biotin on surface potential is illustrated in Fig. 12.11. The topography and KPFM images of a surface patterned with biotin are shown in Figs. 12.11a and c, while the changes in topography and surface potential after the binding of avidin are shown in Figs. 12.11b and d. Comparing the KPFM images before and after the binding, it is clear that the addition of avidin causes the surface potential of the biomolecular region to invert with respect to the background. The topographic and surface potential images of the sample before and after neutravidin exposure are shown in Figs. 12.11e and h. In this case, the potential does not appear to have been affected significantly by the addition of neutravidin. These differences are further illustrated in Figs. 12.11i and j which show cross sections of the potential images. The presence of the charged avidin molecule (see Fig. 12.8) is detectable by KPFM.

In another example of using KPFM to measure changes in surface potential due to the formation of specific biomolecular complexes, Sinensky and Belcher used patterned DNA probe strands taken from anthrax and exposed the DNA to

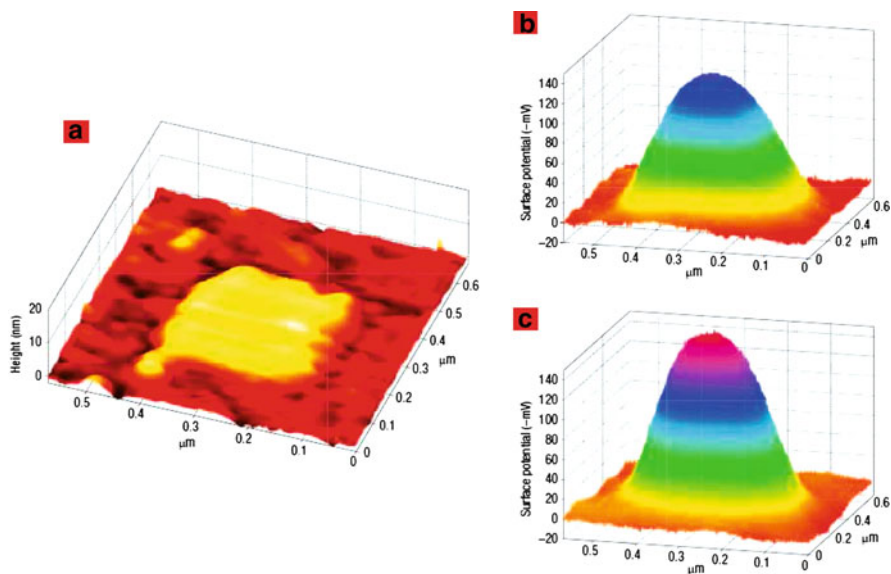


Fig. 12.12 (a) Topography image of a dip pen lithography-patterned anthrax DNA probe. (b) and (c) KPFM images before and after exposure to the complementary anthrax DNA sequence, respectively. Reproduced with permission from [113]. Copyright 2007, Nature Publishing Group

complementary and noncomplementary DNA targets [113]. When a micron-sized anthrax probe is exposed to its complementary target, the surface potential doubles, but when the anthrax probe is exposed to a noncomplementary malaria target no change in surface potential is observed. The same result is observed with a malaria DNA probe; only the complementary target leads to a surface potential doubling. In Fig. 12.12, KPFM results are shown before and after DNA hybridization for a submicron anthrax probe. In this case, surface potential doubling is not observed most likely resulting from the reduced concentrations for small features [113]. Note that the negative surface potential of DNA has been corroborated by other studies [103]. The authors further explored the scan rate and height dependence on the KPFM signal, noting the measurements must be performed close (10s of nm) to the sample surface to achieve high sensitivity and resolution, while the scan rate could be increased from $1 \mu\text{m/s}$ to $1,172 \mu\text{m/s}$ and still resolve micron-sized features, demonstrating the potential for nanoarray analysis by KPFM.

Gao and Cai have taken this approach one step further by demonstrating the potential of KPFM as a tool to detect interactions between DNA and proteins [114]. They used an AFM nanolithography approach to create protein patterns of lysozyme. When the lysozyme is incubated with an anti-lysozyme aptamer, the aptamer binds to the edge of the lysozyme, but when incubated with a randomly generated DNA strand, there is no binding to the lysozyme. KPFM was used to study this aptamer–lysozyme binding using a high aspect ratio Ag_2Ga needle tip.

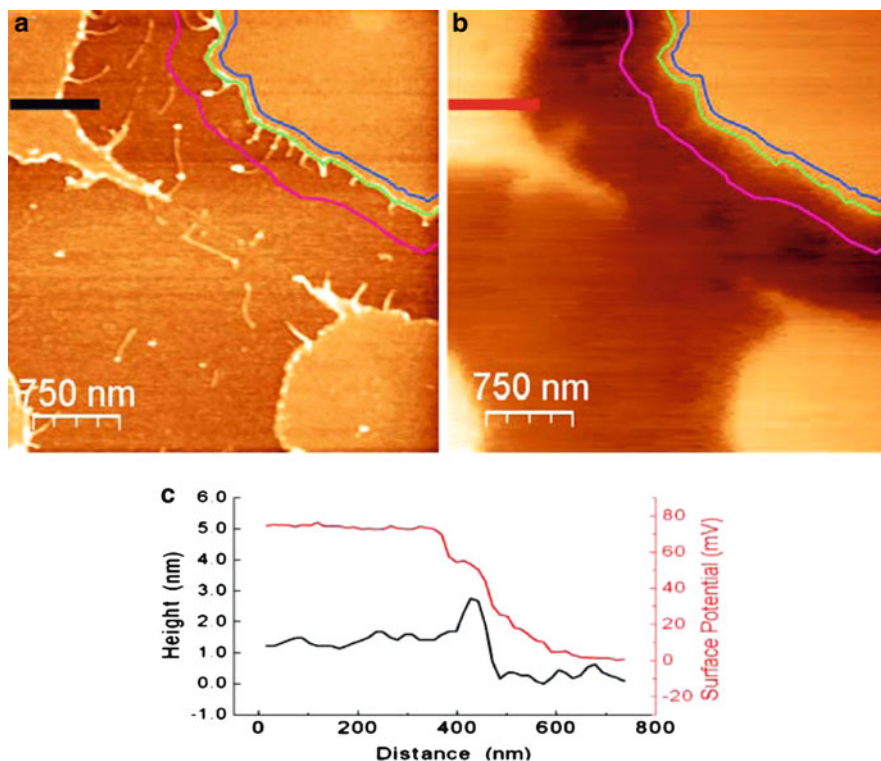


Fig. 12.13 (a) Topography and (b) surface potential images of the lysozyme pattern after incubation with aptamers. (c) Line profiles of the topography and surface potential across the aptamer-lysozyme complex. Reproduced with permission from [114]. Copyright 2009, Springer

Topography and KPFM images of the aptamer-incubated lysozyme patterns are shown in Fig. 12.13. As demonstrated by the line profiles of the topography and KPFM images (Fig. 12.13c), the peak in the topography due to the aptamer-lysozyme complex corresponds to a step in the surface potential. The surface potential of the complex is lower than that of the lysozyme itself and higher than that of the substrate. The authors state that this step was not visible using conventional KPFM tips. Analysis of the surface potentials reveals a 12 mV difference between the lysozyme and the aptamer-lysozyme complex. Richards et al. used KPFM to characterize the functionalization of GaP(100) surfaces with linker molecules and single strand and complementary DNA [200]. They showed a certain tunability in the modification of the surface potential of the GaP surface by varying the initial concentration of the linker molecule.

12.2.2.3 KPFM of Light-Induced Phenomena

KPFM has also been extended to detect changes in surface potential as a result of illumination in optically active proteins and protein membranes. Lee et al.

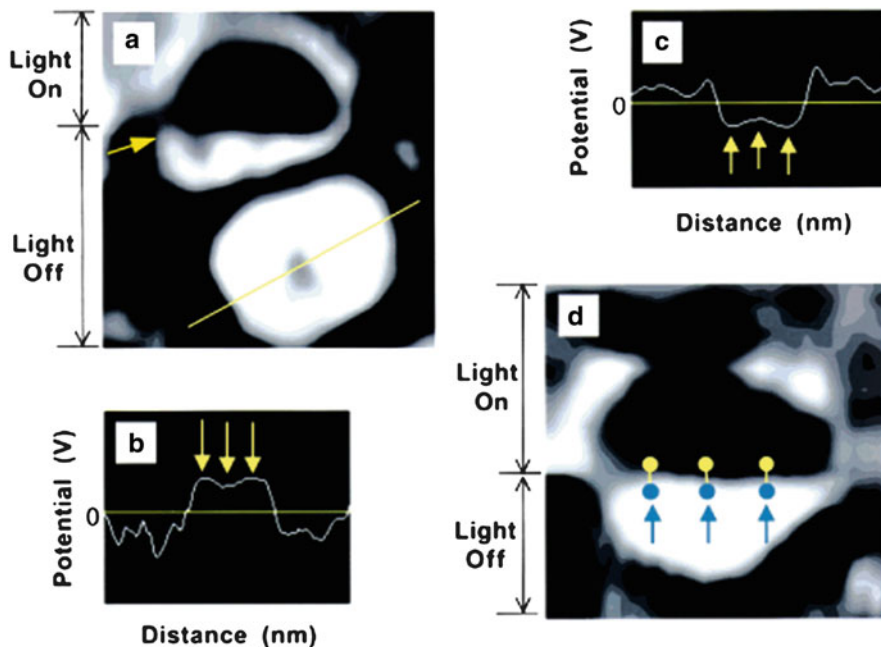


Fig. 12.14 (a) KPFM image of two photosynthetic reaction centers. (b,c) Dark and illuminated voltage-distance profiles, respectively, along the indicated line in (a). In (d) the illumination is turned off mid-scan during the acquisition of the KPFM image of a single reaction center. Reproduced with permission from [115]. Copyright 2000, American Chemical Society

demonstrated the potential of KPFM for the measurement of photovoltages generated from single photosynthetic reaction centers on an organosulfur molecular layer coated, gold coated mica substrate as a function of illumination [115]. They report a reversal of the potential from positive to negative upon illumination while the topography remains unchanged. KPFM images of a photosynthetic reaction center are shown in Fig. 12.14. In Fig. 12.14a the lower reaction center was imaged in a dark state. Line profiles for this reaction center are shown in Figs. 12.14b and c in darkness and under illumination, respectively, showing the potential reversal. In Fig. 12.14d, a single reaction center is shown which is imaged partially under illumination. Frolov et al. extended this approach by demonstrating that a photoelectronic device could be fabricated by direct binding of a reaction center onto a metallic substrate without the need for a surfactant and without losing the capacity to generate a photovoltage [116]. The group of Lee has also used KPFM to investigate reaction center proteoliposomes [117], the air-liquid interface of liquid containing proteoliposomes [118], and bacterial spores [119].

Bacteriorhodopsin, the light-driven protein pump in the purple membrane of *Halobacterium salinarium* has also been investigated by KPFM [120, 121]. Knapp et al. reported KPFM of the purple membrane on mica and HOPG substrates [120].

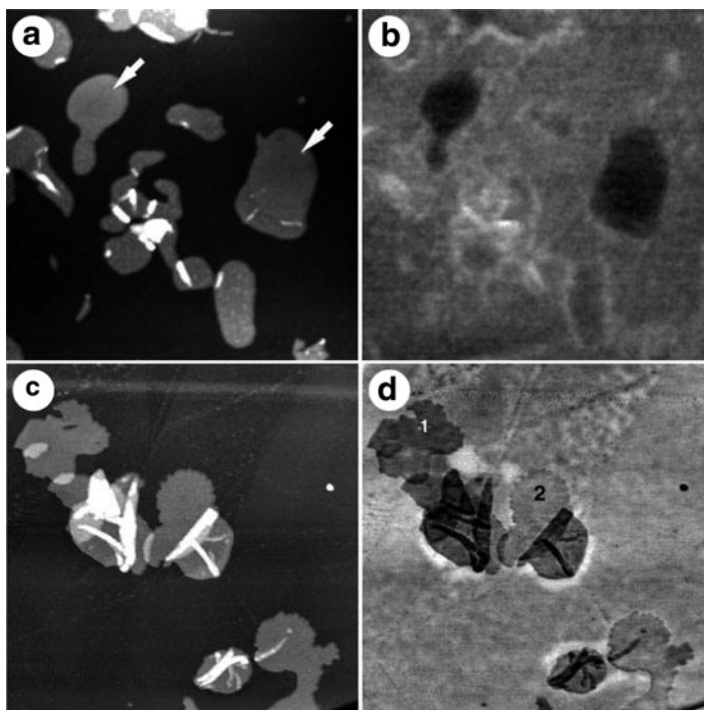


Fig. 12.15 (a) Topography and (b) surface potential of purple membrane imaged on mica at 64% relative humidity ($5.5 \mu\text{m} \times 5.5 \mu\text{m}$). (c) Topography and (d) surface potential of purple membrane imaged on HOPG at 41% relative humidity ($5.3 \mu\text{m} \times 5.3 \mu\text{m}$). Reproduced with permission from [120]. Copyright 2002, John Wiley & Sons, Inc

Topography and surface potential images of purple membrane are shown in Fig. 12.15 for mica (Fig. 12.15a, b) and HOPG (Fig. 12.15c, d). They found the surface potential of the extracellular side of the purple membrane to be more negative than the cytoplasmic side. Knapp et al. also measured the patch voltage of representative patches relative to the HOPG background as a function of illumination, reporting that the extracellular patch surface potential increased by 3–5 mV while the cytoplasmic patch potential decreased by 3–5 mV under illumination. Lee et al. measured surface potentials of the extracellular side of wild type and mutant bacteriorhodopsin membranes at a relative humidity of 65–70% as a function of illumination and buffer solution pH, reporting photoinduced surface potentials of 63 mV and 37 mV for the mutant and wild types, respectively, at pH 10.5 and 48 mV and ~ 0 mV at pH 7 [121].

While surveying the use of KPFM for the characterization of biological systems, we have explored KPFM to look at single molecules, proteins, biomolecular complexes, and most recently patches of membrane protein. Beyond these systems, KPFM has been used to study surface potential mapping in lipid bilayer systems

[122, 123, 125] the primary component of cellular membranes. Leonenko et al. have used KPFM to study the mixed lipid protein pulmonary surfactant that assembles at the air-lung interface [122]. The surface potential at this interface may have relevance to the interaction between airborne particles and surfaces of the lung. Topography and surface potential images of pulmonary surfactant deposited on a mica substrate are shown in Fig. 12.16. Figures 12.16a and b, and are measured without added cholesterol, while Figs. 12.16c–f are surfactant films with 5% cholesterol (by weight). The observed contrast in Fig. 12.15b is explained in terms of the arrangement of stacks of lipid bilayers and their associated dipoles. The monolayer regions are dark (~ -0.6 V) and relatively uniform, while the topographic features are generally less negative. In contrast, for the surfactant-containing cholesterol, the monolayer region appears to show some segregation into domains of different surface potential. It is suggested that a similar effect could be involved in sphingolipid-cholesterol rafts of the plasma membrane. The effect of cholesterol and surfactant protein C on surfactant assembly and surface potential is studied in more detail in [123, 124] and [125], respectively [201]. Recently, the group has explored the differences between different KPFM techniques for characterizing the surface potentials of biomolecular films [200].

12.3 PFM of Biosystems

12.3.1 *Historical Background*

Many biological materials are piezoelectric due to the combination of polar bonds and optical activity inherent to all biopolymers. Electromechanical properties (triboelectricity) ascribed to piezoelectric properties were first demonstrated in biological materials in 1941 [126], and subsequently, the piezoelectric effect was identified in a wide variety of biomaterials including bone, tendon, skin, tooth dentin, blood vessel walls, myosin, actin, amylose, chitin, fibrin, wood cellulose, and DNA [127–131]. The first published report on piezoelectricity in bone in 1957 by Fukada and Yasuda [132] sparked intense research on bone piezoelectricity [133, 134], and it was speculated that piezoelectricity could be responsible for the formation and regeneration of calcified tissues [135, 136]. The organizational complexity of bone [137] and limitations in characterization had sidelined this area of investigation (e.g., the symmetry of piezoelectric response could not be determined absolutely, and minute changes in sample preparation yielded changes in the measured coupling constants) until the advent of AFM-based techniques for electromechanical measurements.

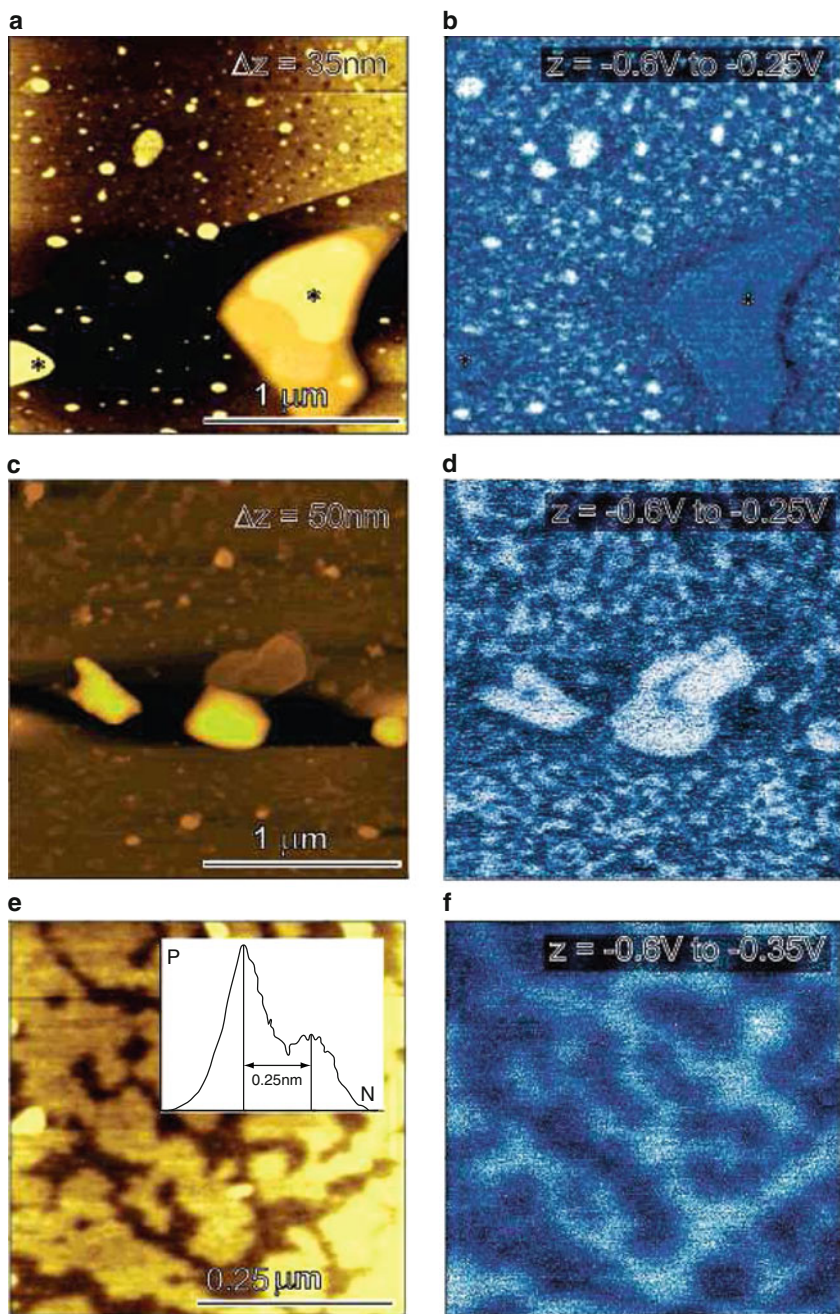


Fig. 12.16 (a), (b) Topography and surface potential images, respectively, of pulmonary surfactant with 0% cholesterol. (c), (e) Topography and (d), (f) surface potential images of pulmonary surfactant with 5% cholesterol. Reproduced with permission from [122]. Copyright 2006, American Chemical Society

12.3.2 PFM of Collagen

In order to understand bioelectromechanics on the nanoscale and to relate piezoelectricity to biological functionality, a nanoscale probe of local piezoelectricity is needed. With recent advances in SPM, it has become possible to investigate piezoelectricity in biological materials at the micro- to nanoscale, and subsequently, piezoelectricity has been measured in a wide variety of calcified and non-calcified connective tissues [138–145]. Recent reports have shown piezoelectricity from single, isolated collagen fibrils [146, 147].

The first nanoelectromechanical measurements of biomaterials were reported by Halperin et al. [138]. They reported piezoelectric values of wet and dry cortical bone and imaged the variation in the response near a Haversian canal (Fig. 12.17). The next advancement came in a series of papers from Kalinin et al., Gruverman et al., and Rodriguez et al. [139–142] where piezoelectric properties of a variety of biosystems including tooth dentin, embedded proteins in enamel, butterfly wing scales, and purified collagen were reported (see [148] for a review).

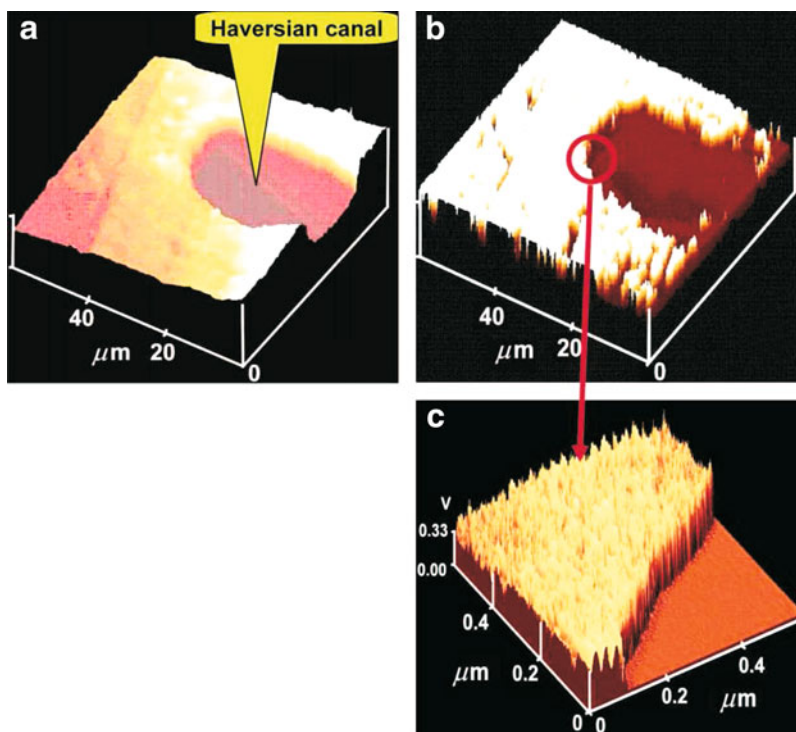


Fig. 12.17 (a) Topography image and (b) and (c) piezoresponse images of mature human cortical bone near the Haversian canal. Reproduced with permission from [138]. Copyright 2004, American Chemical Society

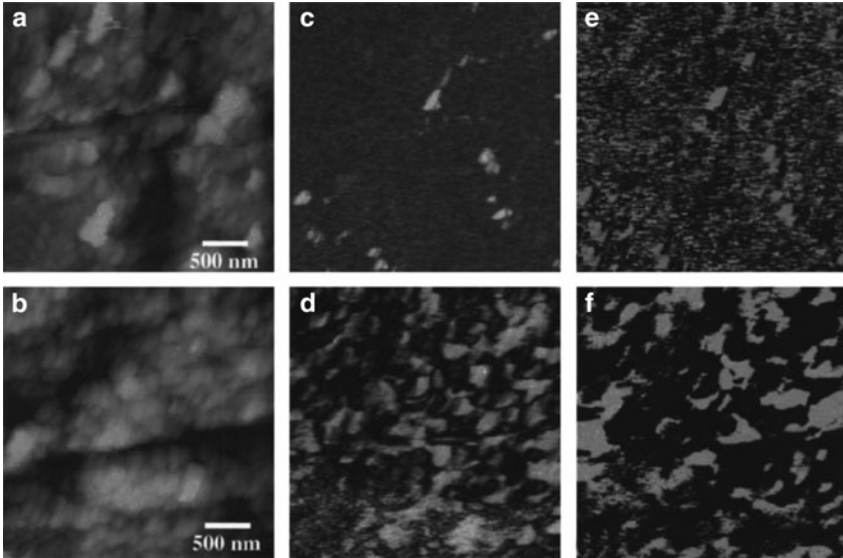


Fig. 12.18 (a), (b) Topographic and (c), (d) PFM amplitude and (e), (f) phase images of human tooth (a), (c), (e) enamel and (b), (d), (f) dentin. Reproduced with permission from [139]. Copyright 2005, American Institute of Physics

The piezoelectric activity in dentin was attributed to the collagen, while that of butterfly wing scales to the protein chitin. Topographic and PFM amplitude and phase images of human tooth enamel and dentin are shown in Fig. 12.18. Recall that the PFM amplitude image provides information on the local piezoelectric activity, while the PFM phase image reveals the orientation of the underlying piezoelectric components. Only isolated response is obtained from the enamel, while analysis of the dentin reveals regions with nearly uniform response having different orientations. As both enamel and dentin contain a hard mineral and a soft protein phase, and the protein content in dentin is much higher than that in enamel, the more uniform response observed in the dentin is attributed to the protein content, primarily type I collagen.

To verify this, Gruverman et al. investigated piezoelectricity in tooth dentin in more detail, using etching to remove the surface mineral component and subsequent bleaching to reveal collagen fibrils [143]. The piezoresponse can clearly be seen to depend on the collagen fibril orientation (Fig. 12.19).

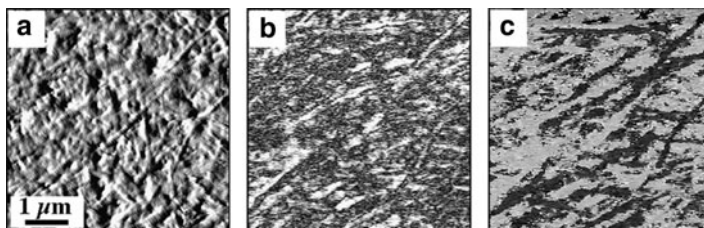


Fig. 12.19 (a) AFM deflection image of an etched and bleached dentin surface. (b) PFM amplitude and (c) phase images of the same dentin surface. Reproduced with permission from [143]. Copyright 2007, Elsevier

Subsequently, Habelitz et al. used PFM to address whether collagen is present in peritubular dentin [144]. Using a combination of VPFM and LPFM and sagittal and occlusal cross sections of tooth dentin, they show a lack of piezoelectricity from peritubular dentin which they attribute to an absence of collagen in the region surrounding the dentin tubules.

These studies focused primarily on piezoelectricity in dental tissues. Recently, Minary-Jolandan and Yu extended PFM to the single collagen fibril [146, 147]. Shown in Figs. 12.20a and b are lateral PFM phase images of a type I collagen fibril. The fibril in Fig. 12.20b has been physically rotated by 180° with respect to Fig. 12.20a and the PFM phase signal has changed accordingly. Figures 12.21a and c show topographic images of a single collagen fibril. The corresponding lateral PFM amplitude images are shown in Figs. 12.21b and d showing apparent intrinsic piezoelectric heterogeneity within a collagen fibril which coincides with the gap and overlap periodicity.

Harnagea et al. analyzed the lateral and vertical response from a fibril in detail, confirming the expected shear piezoelectricity in collagen fibrils, and attributing vertical signal to cantilever buckling [149]. Piezoelectricity in fibrils of type I collagen has been attributed to the hexagonal packing of collagen monomers in a fibrillar structure with periodicity arising from the stacking of the monomers; however, it should be noted that collagen in non-fibrillar form also exhibits piezoelectricity [142]. In Fig. 12.22, PFM images of purified type I collagen in non-fibrillar form deposited on a platinized silicon substrate are shown.

12.3.3 PFM of Other Biosystems

The use of PFM to investigate electromechanical coupling in biosystems has not been limited to biopolymers such as collagen, but has also been applied to systems such as tobacco mosaic viruses (TMVs) [150]. The observed PFM contrast of TMVs was analyzed in terms of topographic crosstalk, differences in elastic properties, and the intrinsic electromechanical coupling due to the piezoelectric and flexoelectric

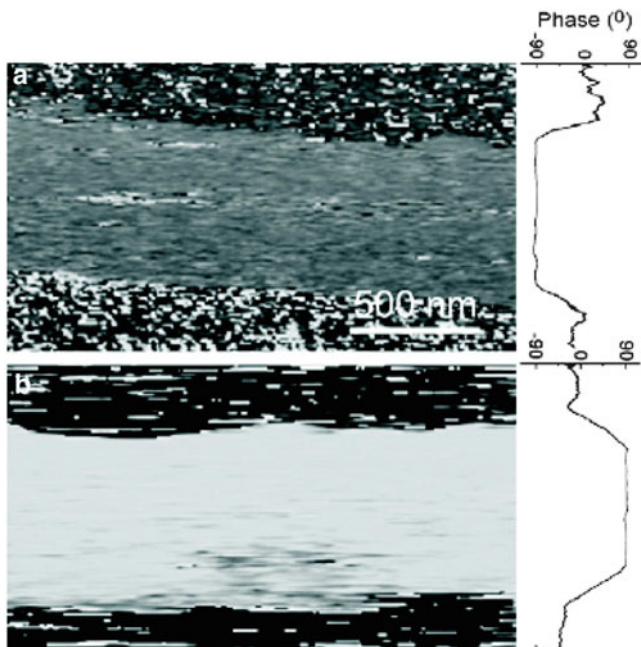
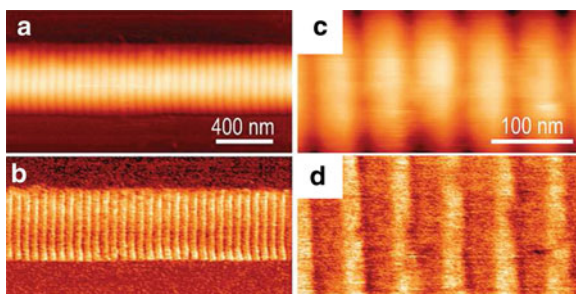


Fig. 12.20 (a) Lateral PFM phase images of a type I collagen fibril (a) before and (b) after the sample was rotated by 180° . Reproduced with permission from [146]. Copyright 2009, Institute of Physics

Fig. 12.21 (a) and (c) Topographic images of a collagen fibril. (b) and (d) lateral PFM amplitude images of the same collagen fibril. Reproduced with permission from [147]. Copyright 2009, American Chemical Society



effects. Kalinin et al. concluded that the contrast was dominated by flexoelectric coupling, and further demonstrated the use of PFM-based techniques for electrical manipulation of these nanosized viruses, as shown in Fig. 12.23, in which one TMV has been removed from a virus network via the application of a dc bias pulse.

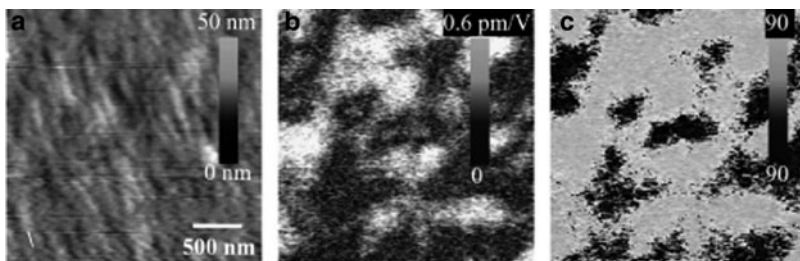
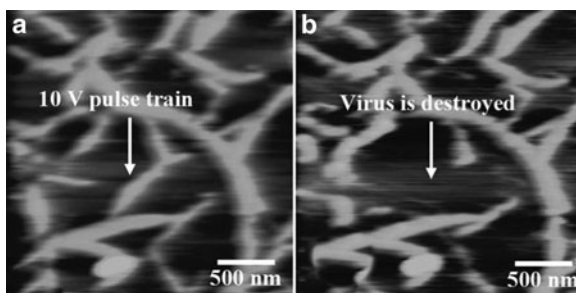


Fig. 12.22 (a) Topography and (b) vertical PFM amplitude and (c) phase images of a type I collagen film deposited on a platinized silicon substrate. Reproduced with permission from [142]. Copyright 2006, Elsevier

Fig. 12.23 Surface topography (a) before and (b) after electrical manipulation of a tobacco mosaic virus. Reproduced with permission from [150]. Copyright 2006, American Institute of Physics



12.3.4 Challenges

A key challenge for electromechanical studies of biopiezoelectrics is the smallness of the coupling coefficients and thereby, the signal-to-noise ratio. Several approaches have been developed to address this issue, as the application of larger bias to elicit a larger response is generally not an option for biological samples. A common solution in dynamic SPMs is to make use of the resonance enhancement of the cantilever to enhance weak mechanical responses. In PFM, this approach was pioneered by Harnagea [151]. However, the use of resonance-enhancement in PFM is limited, since variations in the tip-sample contact stiffness can cause strong coupling between the topography and the apparent PFM signal, making data interpretation difficult. This has led to the development of dual-frequency [152] and band excitation (BE) [153] PFM modes and dual-cantilever systems [154] to increase the signal-to-noise ratio. The use of BE-PFM of ferroelectric materials has been summarized in recent publications [155, 156].

12.4 Liquid Imaging

The obvious challenge for electromechanical and electrostatic SPM measurements of biological systems is imaging in a liquid environment. While the combination of liquid imaging with voltage-modulated SPM techniques seems at first to be a mismatch, the convergence has come from two directions, namely the strong reduction of the adhesive van der Waals force and the absence of capillary forces in liquids, and the necessity to maintain a natural environment for viable biological systems. Note that for imaging in an ambient environment, the van der Waals and capillary forces and the associated jump-to-contact instability separate the “contact” regime with large system stiffness (where electromechanical responses dominate) and the “noncontact” regime with low sample stiffness (where electrostatic forces dominate), a division largely absent in liquids. The second aspect that naturally arises in the context of voltage modulation methods in conductive media is the propensity of these systems for ionic diffusion and electrochemical reactions even at modest ($\sim 1\text{--}2$ V) potential. In comparison, driving voltages in PFM and KPFM are often in the 2–10 V range, suggesting the possible contribution of electrochemical reactions to the imaging process.

At the same time, electric forces in solution play an important role in, e.g., electrical double layers, lipid membranes, and biomolecules [157, 158]. Electric forces in solution are used for a variety of applications, including trapping and manipulating cells and viruses at the microscale [159, 160] and nanofabrication through electrophoretic [161] and electrostatic [162] assembly. Electrostatic interactions are dominated by non-dissipative capacitive forces in ambient [45]. In liquid, complex effects due to electrical double layers, electrochemical reactions, mobile ions, ionic currents, and convective motion of the liquid must be taken into account [163, 164], necessitating experimental methods to probe electrically driven force interactions in liquids.

In this section, efforts to measure electrostatic and electromechanical interactions in a liquid environment are discussed in detail, from attempts to measure electrostatic forces using force distance curves, to voltage-modulated approaches, and to electromechanical imaging of biopolymers in solution.

12.4.1 *Measurements of Electric Potential in Solution*

As outlined in Sect. 12.2, KPFM has recently been applied to the study of surface potentials and electrostatic interactions in biological systems in air and as a function of relative humidity. In general, proteins, biopolymers, and cells are soft materials, and tapping mode in air can be quite destructive to the sample due to the high forces involved, provided the sample remains intact in air. In addition, functional properties can become inactive for certain biological samples imaged in air and also depending on the support or substrate. Also, capillary forces due to the presence of surface

water layers are detrimental to resolution. Similarly, the resolution of electrostatic and surface potential measurements can be limited due to long-range electrostatic forces, which interact with not only the tip locally, but also the entire probe and cantilever beam non-locally. Tapping mode in liquid [165] overcomes some of these limitations and allows for improved resolution and imaging with lower forces. Ideally, only a true noncontact technique would guarantee minimal surface damage. Perhaps more importantly, the role of surface potential and electrostatics in biosystems are most relevant in physiological environments. Interestingly, tapping mode AFM in liquid has been used to visualize surface charge as early as 1998 [202].

Several attempts have been made to measure and analyze electrostatic interactions of biosystems in liquid including force distance mapping and electrostatic balancing with electrolyte solution [166–168]. Müller et al. have used electrostatic balancing with pH and electrolyte solution to improve topographic images of biomolecular membranes [169]. By varying the ionic strength and noting the differences between each image, Philippsen et al. were able to generate difference maps that revealed the electrostatic potential of transmembrane channels [170]. Sotres and Baró used a similar, albeit spectroscopic, mapping approach to measure isodistance maps of the electrical double layer forces of a DNA molecule [171]. Similar approaches based on chemical force microscopy and spectroscopy with functionalized tips have also been used to determine electrostatic forces [172, 173].

Recently, several attempts by the group of Hafner have been made to measure electrostatic forces (charge density maps) of lipid bilayers and DNA in 1–3 mM ionic concentrations using a lift-mode approach [174–176]. In the first line scan, the topography is measured, and in the second, the topography is retraced at a certain constant lift-height from the sample surface (Fig. 12.24a). By choosing the appropriate lift-height for the concentration used, the second line scan will be affected only by the electric double layer. Note that an electrical bias is not applied and the cantilever is not conducting. Through careful calibration of the probe used, the measurement can be made quantitative [175, 176]. A numerical simulation of the field distribution for a tip in an electrolyte solution near a mica-support lipid bilayer film is shown in Fig. 12.24b, and simultaneously-obtained topography and charge density map images of lipid domains are shown in Figs. 12.24c and d.

In KPFM, a dc bias is applied to minimize electrostatic forces or force gradients. As such, to implement KPFM in solution, a dc bias will need to be applied in solution. The application of nonlocal dc bias in solution has been used by Müller and Engel to visualize voltage-gated closure of ion channels by AFM, as shown in Fig. 12.25 [177], and the application of nonlocalized and localized dc bias has been demonstrated for ferroelectric switching [178] by direct biasing of the tip. Insulating conductive probes have also been used to image membranes during the application of bias to a conducting substrate [179].

There are very few examples of voltage-modulated EFM or KPFM imaging in solution. Hirata et al. reported a slightly modified KPFM, electrochemical AFM hybrid for the measurement of surface potential of a mixed, self-assembled thiol film on gold in water [180]. Lynch et al. have used dielectrophoretic force

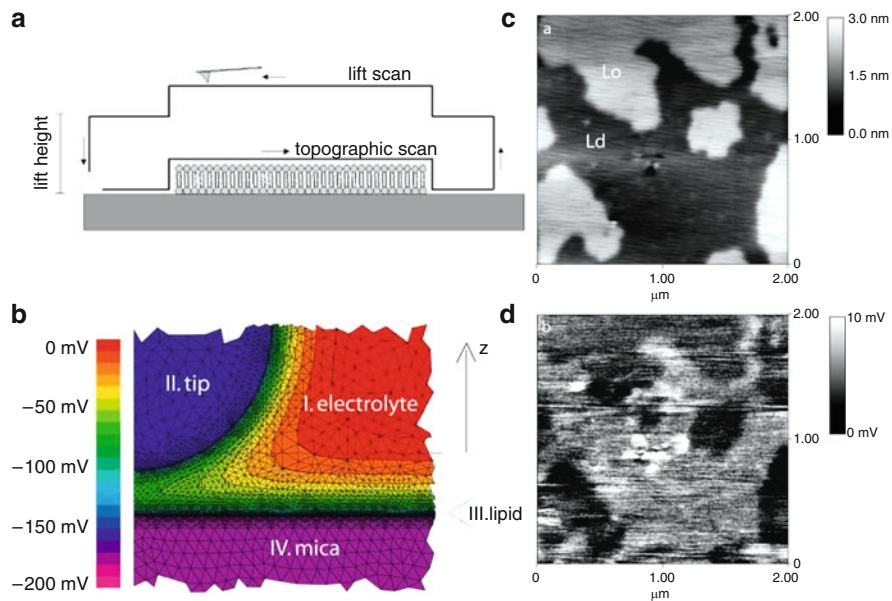


Fig. 12.24 (a) Schematic showing the tip path during lift-mode liquid EFM. (b) Numerical simulations of the tip-sample interaction in an electrolyte solution. (c) Surface topography image of liquid ordered (L_o) and liquid disordered (L_d) lipid domains. (d) Liquid EFM image of the charge density map of the same location demonstrating that the L_o phase is more positive than the L_d phase. Panel (a) reproduced with permission from [174]. Copyright 2003, American Chemical Society. Panels (b–d) reproduced with permission from [175]. Copyright 2007, the Biophysical Society

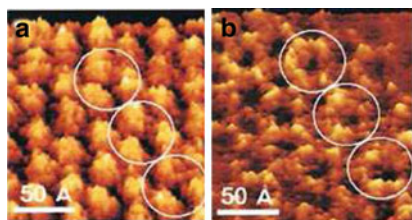


Fig. 12.25 Trigonally packed porin trimers (a) before and (b) after the application of a membrane potential demonstrating a voltage-induced conformational change. Reproduced with permission from [177]. Copyright 1999, Elsevier

microscopy with conducting, biased tips to measure local membrane capacitance of *Escherichia coli* cells in water [181]. Using an approach similar to scanning impedance microscopy (SIM) [182, 183], alternating electrostatic forces have also been measured in a liquid environment using SPM with an ac bias applied to the tip and a microelectrochemical cell formed by two periodically biased electrodes [51].

The implementation of traditional KPFM in solution requires both the application of ac and dc biases with concomitant suppression of unwanted electrochemical processes at the tip–surface junction. The strategies to achieve this goal include the development of insulated and shielded probes (reducing the electrochemically active areas), the use of materials with high overpotentials for water dissociation, and the use of high frequencies. The latter approach can be extended to the use of intermodulation techniques, in which the information on nonlinear (in bias) forces is acquired through the frequency mixing between two high-frequency signals. Additionally, SPMs based on the use of ionically conductive solution [184–186] can potentially be developed to probe bias-induced strain effects. Approaches based on scanning electrochemical potential microscopy may also prove relevant [187]. Finally, one of the most promising techniques is based on a KPFM technique which measures surface potential without using a bias-voltage feedback [203]. This dual-harmonic approach has already been used in a liquid environment [204].

12.4.2 Piezoresponse Force Microscopy

Future work in the area of relating PFM to biofunctionality necessitates electromechanical imaging in a liquid environment. As a first step in this direction, PFM imaging of a ferroelectric sample has been demonstrated in a liquid environment [51]. Both long-range electrostatic forces and capillary interactions were minimized in liquid, resulting in a localization of the ac field to the tip–surface junction and allowing 3 nm resolution to be achieved. PFM images in liquid of a lead zirconate titanate bulk ceramic surface are shown in Fig. 12.26.

As shown previously in Figs. 12.2c and 12.2d, the capacitive tip–surface electrostatic interaction in ambient is present for both noncontact and contact modes of operation, while electromechanical coupling is present only in the contact mode [double arrow in Fig. 12.2d]. In liquid, however, the PFM contrast is strongly mediated by the presence of mobile ions that screen electrostatic tip–surface interactions. For the sphere-plane system [188],

$$F_{\text{el}}^l(z) = \frac{\epsilon\epsilon_0 R}{\lambda_D} \frac{2V_t V_s \exp(h/\lambda_D) - (V_t^2 + V_s^2)}{\exp(2h/\lambda_D) - 1}. \quad (12.3)$$

Electrostatic interactions in liquid are short-range due to screening by mobile ions and decay exponentially for $h > \lambda_D$ (Fig. 12.27a, b). Thus, the electrostatic contribution to the PFM signal in liquid is (for $h > 0$)

$$\text{PR}_{\text{el}}^{\text{liq}} = \frac{\epsilon\epsilon_0 R}{\lambda_D} \frac{2V_s \exp(h/\lambda_D)}{\exp(2h/\lambda_D) - 1} \frac{1}{k_1^l + k}, \quad (12.4)$$

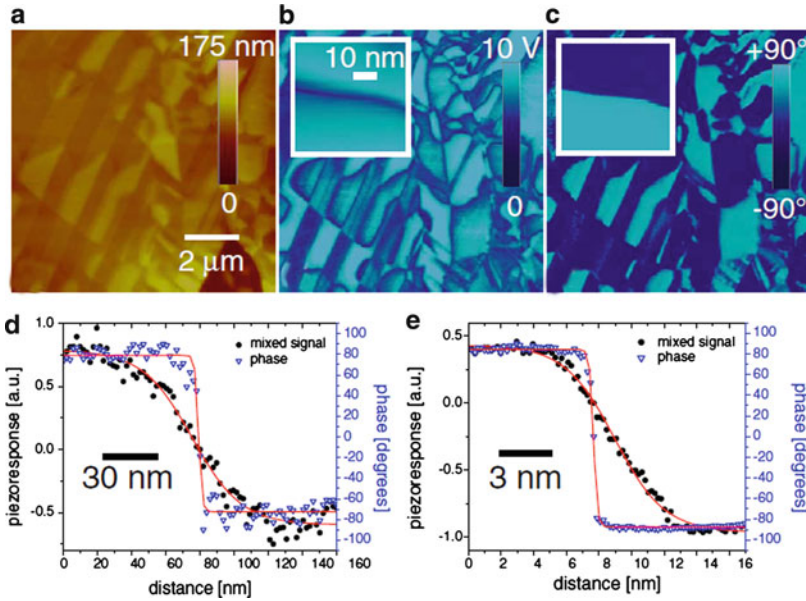


Fig. 12.26 (a) Topography, (b) PFM amplitude, and (c) PFM phase images of a lead zirconate titanate ceramic measured in water. Insets show high resolution PFM images. Domain wall cross-sections of PFM signals in (d) air and (e) water. Reproduced with permission from [51]. Copyright 2006, American Physical Society

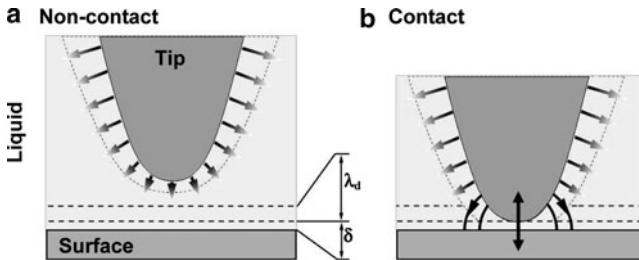


Fig. 12.27 (a) For noncontact SPM techniques, electrostatic forces are minimized in liquid. (b) In contact mode, electrostatic forces are also minimized in liquid; however, electromechanical coupling [double arrow in (b)] is present. The reduced electrostatic force allows improvements in PFM resolution in liquid. Adapted with permission from [51]. Copyright 2006 by the American Physical Society

where k_1^l is tip–surface spring constant in liquid. The contribution from the conical part of the tip and cantilever is absent for $R \gg \lambda_D$. Note that the increase in response observed at the contact point in liquid is due to additional electrostatic coupling in the double layer. The response decreases with increasing force due to the increased contact stiffness.

The electromechanical response in liquid is described by (12.1), where the tip–surface spring constant now includes the effect of the liquid layer. The screening coefficient is $\alpha(h) = 1$ in (12.1) for $h \ll \lambda_D$, i.e., when the tip touches the surface, and is $\alpha(h) = 0$ if the electric double layers around the tip and the surface do not overlap. Thus, the electromechanical response (12.1) in solution gradually decays at distances on the order of the Debye length of the solution, and the electrostatic contribution is significantly minimized as compared to ambient or vacuum imaging (Fig. 12.27b).

Through the application of an ac bias in ambient or liquid environments, the electromechanical coupling can be investigated. In the case of ferroelectric materials in an ambient environment, an applied dc voltage of sufficient magnitude will lead to the nucleation of a ferroelectric domain directly under the tip. In solution, a transition of ferroelectric switching behavior from localized to uniform switching depending on the choice of the solvent has been observed, establishing that imaging is possible at conductivities far larger than allowed for localized switching [178]. Furthermore, these results illustrate the degree to which the spatial extent of a dc field can be controlled in solution. Through the choice of solvent and bias magnitude and duration, it has been shown that it is possible to nucleate a single domain, switch an entire sample surface, and even partially switch a large region (Fig. 12.28). Application of local dc pulses using conventional metal-coated cantilevers is possible only in less conductive nonaqueous solvents such as isopropanol or methanol, which has relevance for the implementation of KPFM in solution.

Liquid PFM has subsequently been applied to a number of biosystems, including lysozyme and insulin fibrils and adenocarcinoma cells [189]. Shown in Fig. 12.29 are topographic and PFM amplitude and phase images of a lysozyme fibril, illustrating the dependence of the measured signal on the applied bias. Note that the topography does not change with bias, while the PFM amplitude signal increases with increasing bias, and the phase response is stronger for higher bias. The fibril does not appear to degrade with repeated scanning or application of ac bias, suggesting the applicability of PFM even on soft biosystems. Some internal structure is discernable in the PFM amplitude images, while the PFM phase response is uniform within a fibril. Similar behavior has been observed for insulin fibrils. The strong dependence of the PFM phase contrast on the driving amplitude and small phase shifts ($\ll 180^\circ$ typical of changes in polar orientation) between dissimilar regions suggest a significant contribution of electric double layer forces and elasticity to the PFM signal. This is not surprising considering most biopolymers are shear piezoelectrics, and the out-of-plane piezoelectric response can be expected to be small. With regards to adenocarcinoma cells, only weak contrast between different cells or at cell boundaries is observed in the PFM amplitude image, while cells with higher height profiles appear to have a slightly different PFM phase response than surrounding cells (not shown). These observations suggest the possibility of a strong elastic contribution to the PFM signal. The high conductivity of the growth media and imaging solution results in uniform biasing of the liquid. To avoid this problem, the imaging should be performed using insulated or shielded probes, in which the central part of the tip is insulated from the solution except

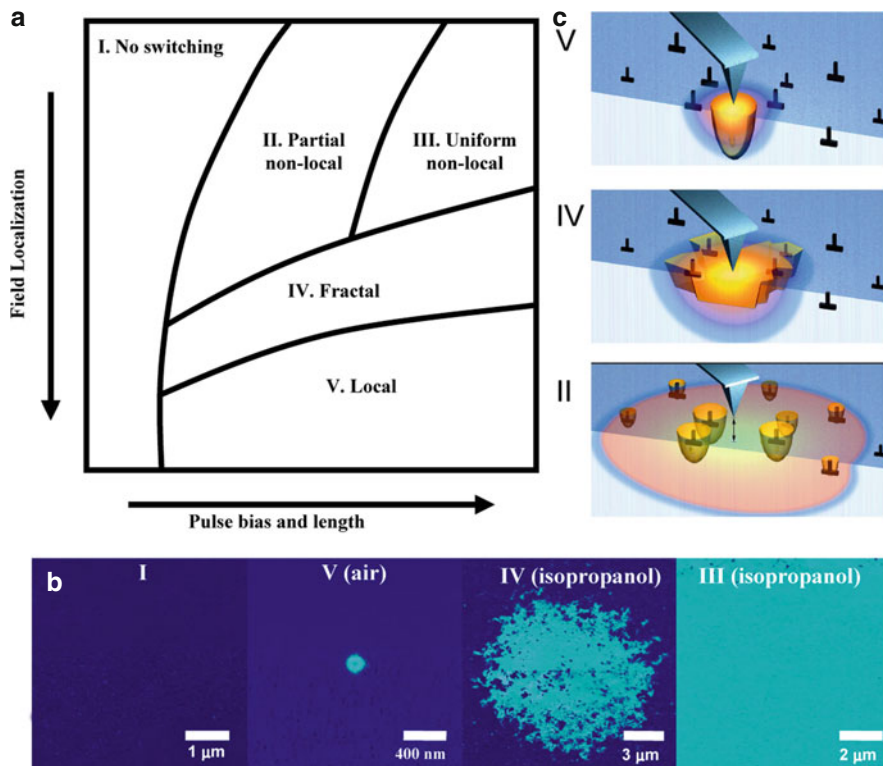


Fig. 12.28 (a) Schematic parameter diagram of possible switching modes vs. field localization and pulse parameters. (b) PFM phase images illustrating domain morphology in regions I, III, IV, and V and the choice of solvent for the phase map in (a). (c) Schematics of switching in local, fractal, and non-local cases. Adapted with permission from [178]. Copyright 2007, American Physical Society

for the region near the probe apex. In addition, a much different response should be expected from electroactive cells such as cardiac myocytes, neuronal cells, and pancreatic beta cells.

There are several major challenges with understanding PFM images in biosystems in solution. First, the electromechanical response depends on the orientation of the polar bonds within the biosystem and the direction the electric field is applied, requiring some knowledge of the biomolecular assembly. Second, the relatively low electromechanical coupling coefficients combined with the potentially reduced signals in solution and complications from topographic crosstalk, differences in elastic properties, other electromechanical couplings such as flexoelectricity in membranes, and the presence of an electrical double layer all make interpretation of the signal and separation of signal components challenging.

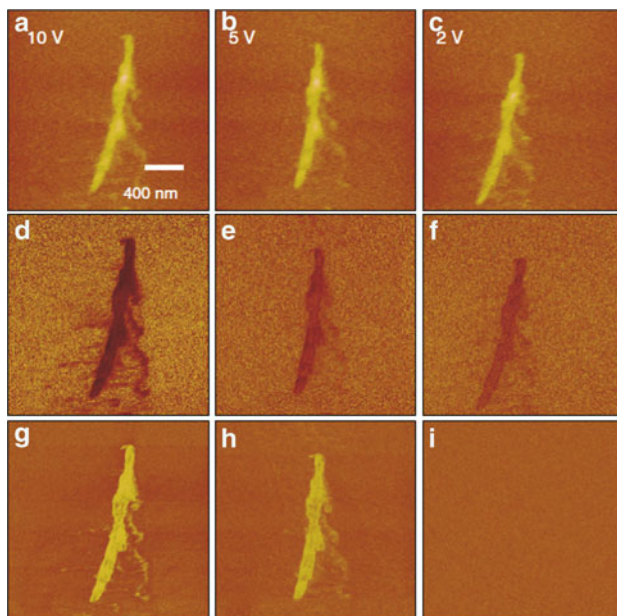


Fig. 12.29 (a–c) Topographic, (d–f) PFM phase, and (g–i) PFM amplitude images of a lysozyme fibril as a function of applied ac bias. Reproduced with permission from [189]. Copyright 2007, Institute of Physics

Nikiforov et al. have begun to address these challenges using BE-PFM in solution. In one instance, they have demonstrated functional recognition imaging of two bacteria types using a combined statistical analysis of the broadband electromechanical response using principal component analysis and a recognition neural network [190]. The technique is demonstrated on model *Micrococcus lysodeikticus* and *Pseudomonas fluorescens* bacteria (Fig. 12.30).

BE-PFM in solution was further applied to study electromechanical coupling in amyloid fibrils [191]. Again, a statistical approach based on principal component analysis is used; this time to separate elastic and electromechanical contributions from the broadband electromechanical signal. The authors demonstrate that in the bulk of the fibril, the electromechanical response is dominated by double-layer effects (consistent with the shear piezoelectricity of biomolecules), while a number of electromechanically active hot spots are observed, possibly related to structural defects, which allow a nonzero out-of-plane piezoresponse. In Fig. 12.31, spatially resolved BE-PFM maps of the electromechanical response amplitude, the quality factor, and resonance frequency are shown.

Beyond these early observations, there are several challenges for the interpretation and applicability of PFM of biosystems in a liquid environment. To explore the biofunctionality of piezoelectricity in biosystems, ideally, the measurements should be performed under physiologically relevant environments; however, it should be

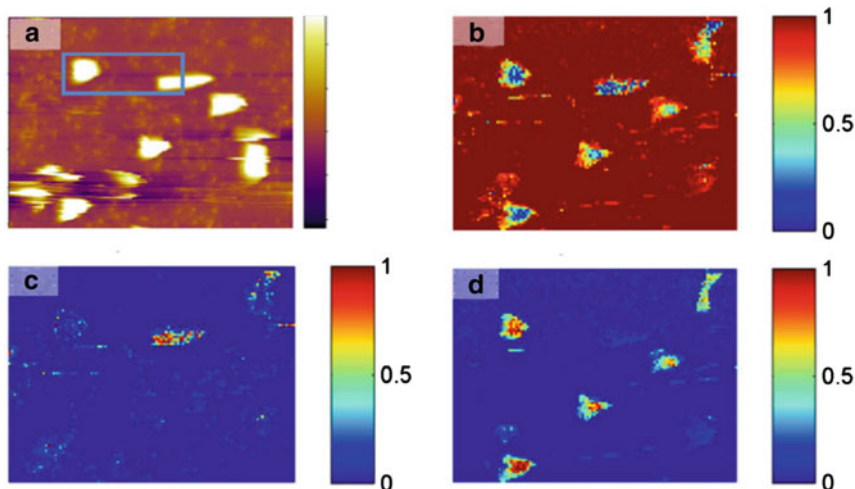


Fig. 12.30 (a) Topography image of bacteria on poly-L-lysine-coated mica. The area within the rectangle in (a) was used to train the neural network. Neural network recognition maps for the (b) background, (c) *P. fluorescens*, and (d) *M. lysodeikticus*. Reproduced with permission from [190]. Copyright 2009, Institute of Physics

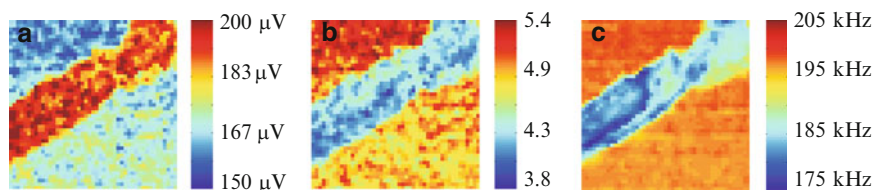
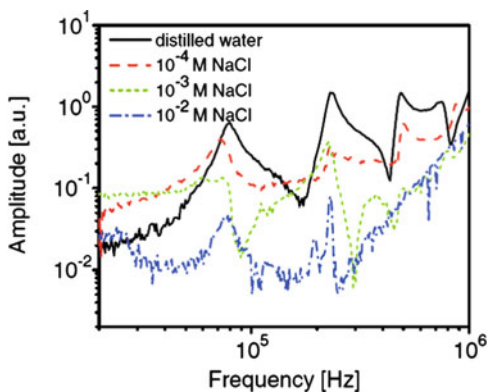


Fig. 12.31 Spatially resolved maps of the (a) amplitude, (b) quality factor, and (c) resonance frequency of electromechanical response of an amyloid fibril. Reproduced with permission from [191]. Copyright 2010, American Chemical Society

noted that the signal in PFM can be reduced significantly in ionic solutions, as demonstrated in Fig. 12.32. Furthermore, biological surfaces in solution are subject to hydration layers which can potentially prevent the detection of shear piezoelectric deformations and limit the bias applied directly to the sample.

As with PFM imaging in air, routes are under investigation to enhance the signal-to-noise ratio for PFM imaging in solution. This is particularly challenging, as a liquid environment is not necessarily compatible with the application of the high bias necessary to increase the signal. Similarly, the use of resonance enhancement in liquid environments is hampered by significant cross-talk between mechanical and electromechanical responses, making data interpretation and quantification difficult.

Fig. 12.32 Piezoresponse amplitude signal as a function of frequency and salt concentration. Reproduced with permission from [51]. Copyright 2006, American Physical Society



12.4.3 At the Intersection of Electrostatics and Electromechanics

The similarities between voltage-modulated electric and electromechanical AFM modes provide a unique opportunity in liquid environments, where the spatial extent of long-range electrostatic forces can be controlled through the choice of the imaging solution. Thus, it may be possible to image electromechanical coupling during the contact portion of the cantilevered tip motion. As such, depending on the imaging medium and parameters, it may be possible to control the image formation mechanism. Several preliminary results are presented below.

In the case of dual-modulation AFM, in which the tip is modulated both mechanically and electrically, it is possible to image a sample in tapping or intermittent-contact and measure information related to the electric or electromechanical interactions. The mechanical motion of the tip is driven at the first free resonance of the cantilever, while the electrical signal is chosen at the second resonance of the cantilever (close to the first contact resonance, as shown in Fig. 12.33b). This approach follows previous implementations of “dual ac” modes [192, 193], but in this case one of the excitations is electrical [42]. This bimodal intermittent contact PFM approach has been first applied to model ferroelectric samples [194]. The approach is outlined schematically in Fig. 12.33, whereby both mechanical and electrical modulations are used (Fig. 12.33a). The piezoelectric response, the effective stiffness, and the electrostatic force (in ambient and liquid environments) are plotted as a function of tip-sample separation in Figs. 12.33c and d.

Shown in Fig. 12.34 are bimodal PFM images of topography and the amplitude of the electromechanical response signal of a purple membrane patch, revealing a change in contrast at features exhibiting topographic contrast. Further work is required to distinguish between electric, elastic, and electromechanical contributions to the signal.

Topography, PFM amplitude, and PFM phase images of human tooth dentin in air are shown in Figs. 12.35a–c, respectively. Intertubular dentin is piezoelectric, while

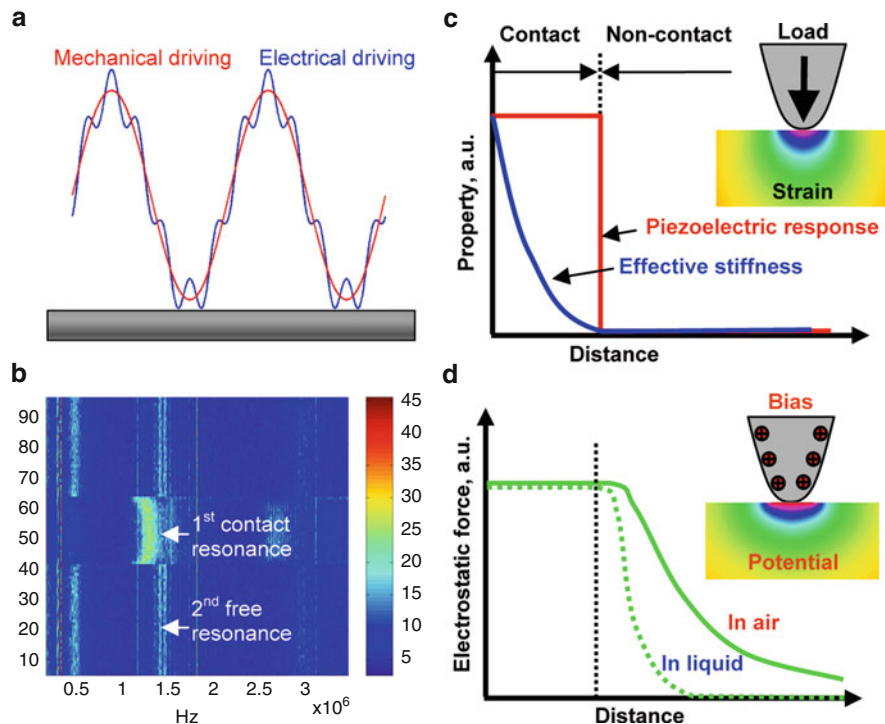


Fig. 12.33 (a) Schematic showing mechanical and electrical modulations. (b) Two-dimensional map of the measured signal as a function of electrical modulation frequency and tip-sample separation. Sketches of (c) the response and effective stiffness as a function of tip-sample separation, and of (d) the electrostatic force as a function of distance in liquid and air. Reproduced with permission from [194]. Copyright 2009, Institute of Physics

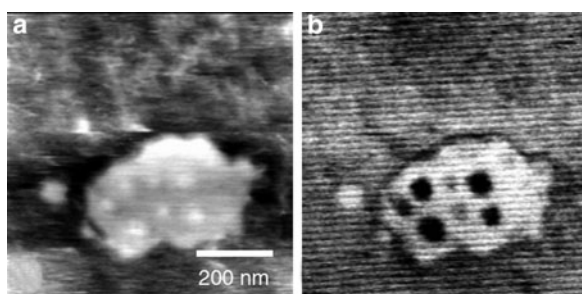


Fig. 12.34 Bimodal PFM mode images of bacteriorhodopsin imaged in buffer solution with a metal coated tip. Shown are (a) surface topography (6 nm z-scale) and (b) the amplitude of the electromechanical response signal. Reproduced with permission from [189]. Copyright 2007, Institute of Physics

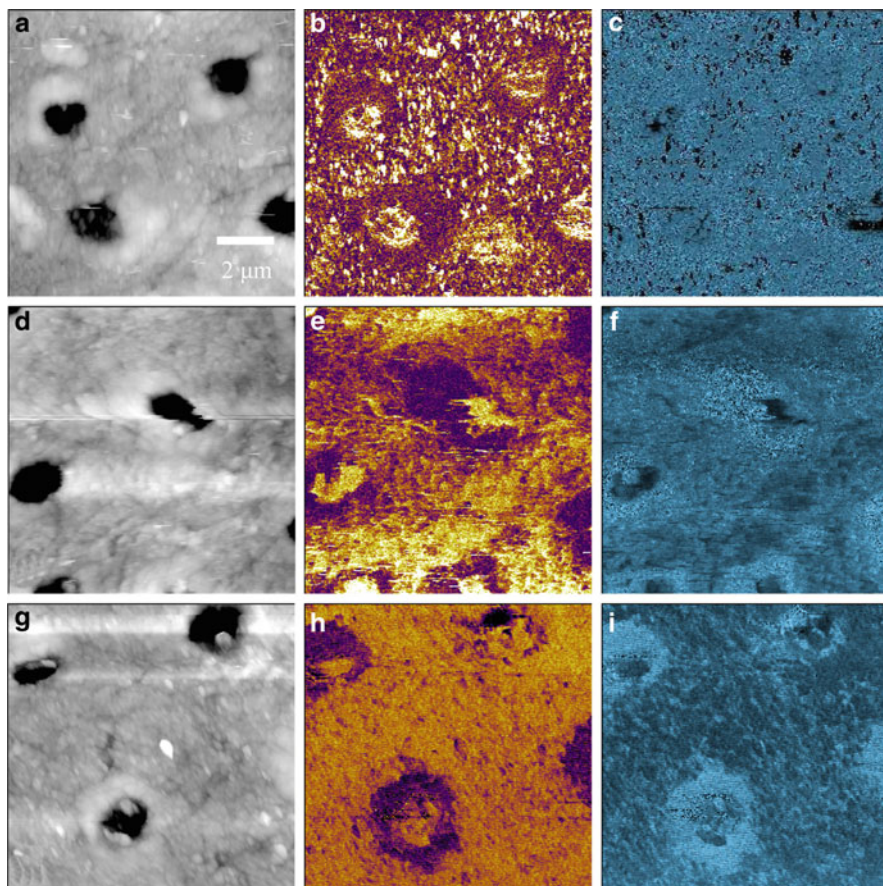


Fig. 12.35 (a), (d), (g) Topography, (b), (e), (h) amplitude, and (c), (f), (i) phase images of dentin in ambient contact mode PFM, liquid contact mode PFM, and liquid bimodal PFM, respectively. Reproduced with permission from [194]. Copyright 2009, Institute of Physics

the peritubular dentin is not, resulting in clear contrast in the PFM amplitude image. Topography, PFM amplitude, and PFM phase images of tooth dentin in deionized water are shown in Figs. 12.35d–f, respectively. The response variations between intertubular and peritubular regions are both still visible. Finally, topography and bimodal PFM images in DI water are shown in Figs. 12.35g–i. While the contrast is further reduced compared to contact mode PFM in liquid, the overall morphology of the intermittent-contact PFM images of dentin is similar to the contact mode PFM, suggesting the feasibility of the approach.

12.5 Summary and Outlook

PFM and KPFM are rapidly emerging as promising techniques for probing electromechanical coupling and electrostatic interactions in biological systems. Dynamic phenomena in biological systems from tissue to cellular, subcellular and molecular levels are typically associated with electromechanical transformations [195]. Thus, PFM and KPFM potentially open pathways for studies of electrophysiology on cellular and molecular levels, signal propagation in neurons, action potentials, etc. Liquid PFM and KPFM may provide novel opportunities for high-resolution studies of imaging biological systems in physiological environments on nanometer and ultimately molecular levels.

Toward this end, there are several challenges that must first be overcome including applying localized bias in solution and separating elastic from electromechanical signals. The former can be addressed through the continued development of probes with electrostatic shielding [164, 179, 196, 197]. The latter can be addressed through the continued development of novel imaging modes [153, 194, 198, 199].

Acknowledgements BJR acknowledges the support of UCD Research and Science Foundation Ireland (grant no. 10/RFP/MTR2855). This research was sponsored (BJR, SVK) by the Center for Nanophase Materials Sciences, Oak Ridge National Laboratory, managed and operated by UT-Battelle, LLC for the Office of Basic Energy Sciences, U.S. Department of Energy.

References

1. B. Honig, A. Nicholls, *Science* **268**, 1144 (1995)
2. A. DeLoof, *Int. Rev. Cytol.* **88**, 251 (1986)
3. R. Plonsey, R.C. Barr, *Bioelectricity: A Quantitative Approach* (Kluwer, New York, 2000)
4. H.G.L. Coster, *J. Biol. Phys.* **29**, 363 (2003)
5. F. Sachs, W.E. Brownell, G. Petrov, *MRS Bull.* **34**, 665 (2009)
6. M. Olivotto, A. Arcangeli, M. Carlà, E. Wanke, *Bioessays* **18**, 495 (1996)
7. M.F. Perutz, *Science* **201**, 1187 (1978)
8. K.A. Sharp, B.H. Honig, *Annu. Rev. Biophys. Biophys. Chem.* **19**, 301 (1990)
9. B.H. Honig, W.L. Hubbell, R.F. Flewelling, *Annu. Rev. Biophys. Biophys. Chem.* **15**, 163 (1986)
10. G.C. Brown, *FEBS Lett.* **260**, 1 (1990)
11. S. McLaughlin, *Curr. Top. Membr. Transp.* **9**, 71 (1977)
12. S. McLaughlin, *Annu. Rev. Biophys. Biophys. Chem.* **18**, 113 (1989)
13. D.S. Cafiso, *Curr. Opin. Struct. Biol.* **1**, 185 (1991)
14. S.S. Strickler, A.V. Gribenko, T. R. Keiffer, J. Tomlinson, T. Reihle, V.V. Loladze, G.I. Makhataдзе, *Biochemistry* **45**, 2761 (2006)
15. C. Tang, J. Iwahara, M. Clore, *Nature* **444**, 383 (2006)
16. T. Yeung S. Grinstein, *Immunol. Rev.* **219**, 17 (2007)
17. T. Yeung, M. Terebiznik, L. Yu, J. Silvius, W. M. Abidi, M. Philips, T. Levine, A. Kapus, S. Grinstein, *Science* **313**, 347 (2006)
18. A.V. Pislakov, P.K. Sharma, Z.T. Chu, M. Haranczyk, A. Warshel, *PNAS* **105**, 7726 (2008)
19. Z. Hejnowics, K. Trebacz, A. Sievers, *Plant Cell. Environ.* **18**, 471 (1995)
20. K.M. Tyner, R. Kopelman, M.A. Philbert, *Biophys. J.* **93**, 1163 (2007)

21. M. Mazzani, J. O. Bustamante, H. Oberleithner, *Physiol. Rev.* **81**, 1 (2001)
22. L. Catacuzzeno, B. Fioretti, F. Franciolini, *Biophys. J.* **95**, 2160 (2008)
23. S. McLaughlin, A. Aderem, *Trends Biochem. Sci.* **20**, 272 (1995)
24. S.D. Zakharov, T.I. Rokistkaya, V.L. Shapovalov, Y.N. Antonenko, W.A. Cramer, *Proc. Natl. Acad. Sci. USA* **99**, 8654 (2002)
25. T.Y. Tsong, R.D. Astumian, *Progr. Biophys. Mol. Biol.* **50**, 1 (1987)
26. T.Y. Tsong, R.D. Astumian, *Annu. Rev. Physiol.* **50**, 273 (1988)
27. T.Y. Tsong, *Annu. Rev. Biophys. Biophys. Chem.* **19**, 83 (1990)
28. D. Oliver, C.-C. Lien, M. Soom, T. Baukrowitz, P. Jonas, B. Fakler, *Science* **304**, 265 (2004)
29. W.A. Catterall, *Annu. Rev. Biochem.* **55**, 953 (1986)
30. M. Grabe, H. Lecar, Y.N. Jan, L.Y. Jan, *Proc. Natl. Acad. Sci. USA* **101**, 17640 (2004)
31. S.V. Kalinin, B.J. Rodriguez, S. Jesse, P. Maksymovych, K. Seal, M. Nikiforov, A.P. Baddorf, A.L. Kholkin, R. Proksch, *Mater Today* **11**, 16 (2008)
32. B.J. Blanchard, V.L. Thomas, V.M. Ingram, *Biochem. Biophys. Res. Commun.* **293**, 1197 (2002)
33. J.S. Kim, L. He, J.J. Lemasters, *Biochem. Biophys. Res. Commun.* **304**, 463 (2003)
34. G.T. Rogers, *J. Appl. Electrochem.* **12**, 379 (1982)
35. M. Levin, *Bioelectromagnetics* **24**, 295 (2003)
36. S.V. Kalinin, B.J. Rodriguez, S. Jesse, B. Mirman, E. Karapetian, E.A. Eliseev, A.N. Morozovska, *Annu. Rev. Mater. Sci.* **37**, 189 (2007)
37. S.V. Kalinin, N. Setter, A. Kholkin, *MRS Bull.* **34**, 634 (2009)
38. K.K. Papachroni, D.N. Karatzas, K.A. Papavassiliou, E.K. Basdra, A.G. Papavassiliou, *Trends Mol. Med.* **15**, 208 (2009)
39. H.M. Frost, *Anat. Rec.* **226**, 403 (1990)
40. G. Binnig, C. F. Quate, C. Gerber, *Phys. Rev. Lett.* **56**, 930 (1986)
41. S. Sadewasser, P. Jelinek, C.-K. Fang, O. Custance, Y. Yamada, Y. Sugimoto, M. Abe, S. Morita, *Phys. Rev. Lett.* **103**, 266103 (2009)
42. B.D. Terris, J.E. Stern, D. Rugar, H.J. Mamin, *Phys. Rev. Lett.* **63**, 2669 (1989)
43. F. Saurenbach, B.D. Terris, *Appl. Phys. Lett.* **56**, 1703 (1990)
44. M. Nonnenmacher, M.P. O'Boyle, H.K. Wickramasinghe, *Appl. Phys. Lett.* **58**, 2921 (1991)
45. T. Glatzel, M.Ch. Lux-Steiner, E. Strassburg, A. Boag, Y. Rosenwaks, in *Principles of Kelvin Probe Force Microscopy*, ed. by S.V. Kalinin, A. Gruverman. *Scanning Probe Microscopy: Electrical and Electromechanical Phenomena on the Nanoscale*, vol. 1 (Springer Science and Business Media, New York, 2007), pp. 113–131
46. C. Leung, H. Kinns, B.W. Hoogenboom, S. Howorka, P. Mesquida, *Nano Lett.* **9**, 2769 (2009)
47. S. Kitamura, M. Iwatsuki, *Appl. Phys. Lett.* **72**, 3154 (1998)
48. C. Loppacher, U. Zerweck, L. M. Eng, *Nanotechnology* **15**, S9 (2004)
49. C. Loppacher, U. Zerweck, S. Teich, E. Beyreuther, T. Otto, S. Grafström, L.M. Eng, *Nanotechnology* **16**, S1 (2005)
50. C. Baumgart, M. Helm, H. Schmidt, *Phys. Rev. B* **80**, 085305 (2009)
51. B.J. Rodriguez, S. Jesse, A.P. Baddorf, S.V. Kalinin, *Phys. Rev. Lett.* **96**, 237602 (2006)
52. A. Gruverman, O. Auciello, H. Tokumoto, *J. Vac. Sci. Technol. B* **14**, 602 (1996)
53. A. Gruverman, O. Auciello, H. Tokumoto, *Appl. Phys. Lett.* **69**, 3191 (1996)
54. T. Hidaka, T. Maruyama, M. Saitoh, N. Mikoshiba, M. Shimizu, T. Shiosaki, L. A. Wills, R. Hiskes, S. A. Dicarolis, J. Amano, *Appl. Phys. Lett.* **68**, 2358 (1996)
55. A. Gruverman, O. Auciello, H. Tokumoto, *Annu. Rev. Mat. Sci.* **28**, 101 (1998)
56. M. Alexe, A. Gruverman (eds.) *Nanoscale Characterization of Ferroelectric Materials*. (Springer, Berlin, 2004)
57. S. Hong, (ed.) *Nanoscale Phenomena in Ferroelectric Thin Films*. (Kluwer Academic Publishers, Norwell, MA, 2004)
58. M. Alexe, C. Harnagea, D. Hesse, U. Gösele, *Appl. Phys. Lett.* **75**, 1793 (1999)
59. M. Alexe, A. Gruverman, C. Harnagea, N.D. Zakharov, A. Pignolet, D. Hesse, J.F. Scott, *Appl. Phys. Lett.* **75**, 1158 (1999)
60. P. Günther, K. Dransfeld, *Appl. Phys. Lett.* **62**, 1137 (1992)

61. S.V. Kalinin, B.J. Rodriguez, S. Jesse, J. Shin, A.P. Baddorf, P. Gupta, H. Jain, D.B. Williams, A. Gruverman, *Microsc. Microanal.* **12**, 206 (2006)
62. A. Roelofs, U. Böttger, R. Waser, F. Schlaphof, S. Trogisch, *L.M. Eng, Appl. Phys. Lett.* **77**, 3444 (2000)
63. L.M. Eng, H.-J. Güntherodt, G. Rosenman, A. Skliar, M. Oron, M. Katz, D. Eger, *J. Appl. Phys.* **83**, 5973 (1998)
64. B.J. Rodriguez, A. Gruverman, A.I. Kingon, R.J. Nemanich, J.S. Cross, *J. Appl. Phys.* **95**, 1958 (2004)
65. S.V. Kalinin, E. Karapetian, M. Kachanov, *Phys. Rev. B* **70**, 184101 (2004)
66. S.V. Kalinin, D.A. Bonnell, *Phys. Rev. B* **65**, 125408 (2002)
67. H. Sugimura, K. Hayashi, N. Saito, N. Nakagiri, O. Takai, *Appl. Surf. Sci.* **188**, 403 (2002)
68. H. Sugimura, N. Saito, N. Maeda, I. Ikeda, Y. Ishida, K. Hayashi, L. Hong, O. Takai, *Nanotechnology* **15**, S69 (2004)
69. J. Lü, E. Delamar, L. Eng, R. Bennewitz, E. Meyer, H.J. Güntherodt, *Langmuir* **15**, 8184 (1999)
70. N. Saito, K. Hayashi, H. Sugimura, O. Takai, N. Nakagiri, *Surf. Interface Anal.* **34**, 601 (2002)
71. T. Ichii, T. Fukuma, K. Kobayashi, H. Yamada, K. Matsushige, *Nanotechnology* **15**, S30 (2004)
72. H. McNally, D.B. Janes, B. Kasibhatla, C.P. Kubiak, *Superlatt. Microstruct.* **31**, 239 (2002)
73. M. Fujihira, H. Kawate, *J. Vac. Sci. Technol. B* **12**, 1604 (1994)
74. L.F. Chi, S. Jacobi, H. Fuchs, *Thin Solid Films* **284**, 403 (1996)
75. M. Fujihira, *Annu. Rev. Mater. Sci.* **29**, 353 (1999)
76. N. Reitzel, T. Hassenkam, K. Balashev, T. R. Jensen, P. B. Howes, K. Kjaer, A. Fechtenkötter, N. Tchebotareva, S. Ito, K. Müllen, T. Bjørnholm, *Chem. Eur. J.* **7**, 4894 (2001)
77. P. Karageorgiev, B. Stiller, D. Prescher, B. Dietzel, B. Schulz, L. Brehmer, *Langmuir* **16**, 5515 (2000)
78. H. Yamada, T. Fukuma, K. Umeda, K. Kobayashi, K. Matsushige, *Appl. Surf. Sci.* **188**, 391 (2002)
79. V. Palermo, M. Palma, Ž Tomović, M. D. Watson, R. Friedlein, K. Müllen, P. Samorì, *Chem. Phys. Chem.* **6**, 2371 (2005)
80. A. Liscio, V. Palermo, D. Gentilini, F. Nolde, K. Müllen, P. Samorì, *Adv. Funct. Mater.* **16**, 1407 (2006)
81. V. Palermo, M. Palma, P. Samorì, *Adv. Mater.* **18**, 145 (2006)
82. V. Palermo, A. Liscio, M. Palma, M. Surin, R. Lazzaroni, P. Samorì, *Chem. Commun.* 2007, 3326 (2007)
83. R. Buhler, W. Sturmer, H.J. Apell, P. Lauger, *J. Membr. Biol.* **121**, 141 (1991)
84. J. Zhang, R.M. Davidson, M.D. Wei, L.M. Loew, *Biophys. J.* **74**, 48 (1998)
85. P. Gogan, I. Schmiedel-Jakob, Y. Chitti, S. Tyc-Dumont, *Biophys. J.* **69**, 299 (1995)
86. L.B. Cohen, B.M. Salzberg, H.V. Davila, W.N. Ross, D. Landowne, A.S. Waggoner, C.H. Wang, *J. Membr. Biol.* **19**, 1 (1974)
87. J.Y. Wu, Y.W. Lam, C.X. Falk, L.B. Cohen, J. Fang, L. Loew, J.C. Prechtel, D. Kleinfeld, Y. Tsau, *Histochem. J.* **30**, 169 (1998)
88. M.S. Siegel, E.Y. Isacoff, in *Green fluorescent proteins for measuring voltage*, ed. by R. Yuste, A. Konnerth. Imaging in Neuroscience and Development: A Laboratory Manual (Cold Spring Harbor Laboratory Press, Cold Spring Harbor, NY, 2005), pp. 573
89. A. Kuznetsov, V.P. Bindokas, J.D. Marks, L.H. Philipson, *Am. J. Physiol. Cell Physiol.* **289**, 224 (2005)
90. J. Gorelik, Y. Gu, H.A. Spohr, A.I. Shevchuk, M.J. Lab, S.E. Harding, C.R.W. Edwards, M. Whitaker, G.W.J. Moss, D.C.H. Benton, D. Sánchez, A. Darszon, I. Vodyanoy, D. Klennerman, Y. E. Korchev, *Biophys. J.* **83**, 3296 (2002)
91. D. Laoudji, C. Guasch, E. Renault, R. Bennes, J. Bonnet, *Anal. Bioanal. Chem.* **381**, 1476 (2005)
92. D.C. Hansen, K.M. Hansen, T.L. Ferrell, T. Thundat, *Langmuir* **19**, 7514 (2003)
93. I.D. Baikie, P.J.S. Smith, D.M. Porterfield, P.J. Estrup, *Rev. Sci. Instrum.* **70**, 1842 (1999)

94. M. Thompson, L.E. Cheran, Faraday Discuss. **116**, 23 (2000)
95. L.E. Cheran, S. Sadeghi, M. Thompson, Analyst **130**, 1569 (2005)
96. L.E. Cheran, M. Chacko, M.Q. Zhang, M. Thompson, Analyst **129**, 161 (2004)
97. M. Thompson, L.-E. Cheran, M. Zhang, M. Chacko, H. Huo, S. Sadeghi, Biosens. Bioelectron. **20**, 1471 (2005)
98. I. Lee, E. Greenbaum, in *Electrical Scanning Probe Microscopy of Biomolecules on Surfaces and at Interfaces*, ed. by S.V. Kalinin, A. Gruverman. Scanning Probe Microscopy: Electrical and Electromechanical Phenomena on the Nanoscale, vol. 2, (Springer Science and Business Media, New York, 2007) pp. 601
99. Y. Leng, C.C. Williams, Colloids and Surfaces A **93**, 335 (1994)
100. A. Gil, P.J. de Pablo, J. Colchero, J. Gómez-Herrero, A.M. Baró, Nanotechnology **13**, 309 (2002)
101. K.J. Kwak, S. Yoda, M. Fujihira, Appl. Surf. Sci. **210**, 73 (2003)
102. E. Mikamo-Satoh, F. Yamada, A. Takagi, T. Matsumoto, T. Kawai, Nanotechnology **20**, 145102 (2009)
103. C. Leung, H. Kinns, B.W. Hoogenboom, S. Howorka, P. Mesquida, Nano Lett. **9**, 2769 (2009)
104. C. Leung, D. Maradan, A. Kramer, S. howorka, P. Mesquida, B.W. Hoogenboom, Appl. Phys. Lett. **97**, 203703 (2010)
105. A. Efimov, S.R. Cohen, J. Vac. Sci. Technol. A **18**, 1051 (2000)
106. R. Ohta, N. Saito, T. Ishizaki, O. Takai, Surf. Sci. **600**, 1674 (2006)
107. L. Fumagalli, G. Ferrari, M. Sampietro, G. Gomila, Nano Lett. **9**, 1604 (2009)
108. G. Gramse, I. Casuso, J. Toset, L. Fumagalli, G. Gomila, Nanotechnology **20**, 395702 (2009)
109. L. Fumagalli, G. Ferrari, M. Sampietro, I. Casuso, E. Martinez, J. Samitier, G. Gomila, Nanotechnology **17**, 4581 (2006)
110. X.Q. Chen, H. Yamada, T. Horiuchi, K. Matsushige, S. Watanabe, M. Kawai, P.S. Weiss, J. Vac. Sci. Technol. B **17**, 1930 (1999)
111. D.C. Coffey, D.S. Ginger, Nat. Mater. **5**, 735 (2006)
112. L. Kronik, Y. Shapira, Surf. Interface Anal. **31**, 954 (2001)
113. A.K. Sinensky, A.M. Belcher, Nature Nanotech. **2**, 653 (2007)
114. P. Gao, Y. Cai, Anal. Bioanal. Chem. **394**, 207 (2009)
115. I. Lee, J.W. Lee, A. Stubna, E. Greenbaum, J. Phys. Chem. B **104**, 2439 (2000)
116. L. Frolov, Y. Rosenwaks, C. Carmeli, I. Carmeli, Adv. Mater. **17**, 2434 (2005)
117. T. Kuritz, I. Lee, E.T. Owens, M. Humayun, E. Greenbaum, IEEE Trans. Nano. Biosci. **4**, 196 (2005)
118. I. Lee, J.W. Lee, A. Stubna, E. Greenbaum, J. Phys. Chem. B **107**, 14225 (2003)
119. I. Lee, E. Chung, H. Kweon, S. Yiacoumi, D.C. Joy, A.V. Palumbo, C. Tsouris, Microsc. Microanal. **15**, 1132 (2009)
120. H.F. Knapp, P. Mesquida, A. Stemmer, Surf. Interface Anal. **33**, 108 (2002)
121. I. Lee, E. Greenbaum, S. Budy, J.R. Hillebrecht, R.R. Birge, J.A. Stuart, J. Phys. Chem. B **110**, 10982 (2006)
122. Z. Leonenko, M. Rodenstein, J. Döhner, L.M. Eng, M. Amrein, Langmuir **22**, 10135 (2006)
123. Z. Leonenko, S. Gill, S. Baoukina, L. Monticelli, J. Doehner, L. Gunasekara, F. Felderer, M. Rodenstein, L. M. Eng, M. Amrein, Biophys. J. **93**, 674 (2007)
124. E. Finot, Y. Leonenko, B. Moores, L. Eng, M. Amrein, Z. Leonenko, Langmuir **26**, 1929 (2010)
125. F. Hane, B. Moores, M. Amrein, Z. Leonenko, Ultramicroscopy **109**, 968 (2009)
126. A. J. P. Martin, Proc. Phys. Soc. **53**, 186 (1941)
127. E. Fukada, J. Phys. Soc. Japan **10**, 149 (1955)
128. V.A. Bazhenov, Piezoelectric Properties of Wood (Consultant Bureau, New York, 1961)
129. H.S. Nalwa, *Ferroelectric Polymers: Chemistry, Physics and Applications* (Dekker, New York, 1995)
130. E. Fukada, R. Prog. Polym. Phys. **38**, 1 (1995)
131. E. Fukada, IEEE Trans. Ultrason. Ferroelectr. Freq. Control **47**, 1277 (2000)
132. E. Fukada, I. Yasuda, J. Phys. Soc. Jpn. **12**, 1158 (1957)

133. E. Fukada, I. Yasuda, *Jpn. J. Appl. Phys.* **3**, 117 (1964)
134. S.B. Lang, *Nature* **212**, 704 (1966)
135. C.A.L. Bassett, *Calc. Tiss. Res.* **1**, 252 (1968)
136. A.A. Marino, R.O. Becker, *Nature* **228**, 473 (1970)
137. S. Weiner, H.D. Wagner, *Annu. Rev. Mater. Res.* **28**, 271 (1998)
138. C. Halperin, S. Mutchnik, A. Agronin, M. Molotskii, P. Urenski, M. Salai, G. Rosenman, *Nano Lett.* **4**, 1253 (2004)
139. S.V. Kalinin, B.J. Rodriguez, S. Jesse, T. Thundat, A. Gruverman, *Appl. Phys. Lett.* **87**, 053901 (2005)
140. S.V. Kalinin, B.J. Rodriguez, J. Shin, S. Jesse, V. Grichko, T. Thundat, A.P. Baddorf, A. Gruverman, *Ultramicroscopy* **106**, 334 (2006)
141. A. Gruverman, B.J. Rodriguez, S.V. Kalinin, *J. Scann. Probe Micros.* **1**, 1 (2006)
142. B.J. Rodriguez, S.V. Kalinin, J. Shin, S. Jesse, V. Grichko, T. Thundat, A.P. Baddorf, A. Gruverman, *J. Struct. Bio.* **153**, 151 (2006)
143. A. Gruverman, D. Wu, B.J. Rodriguez, S.V. Kalinin, S. Habelitz, *Biochem. Biophys. Res. Commun.* **352**, 142 (2007)
144. S. Habelitz, B.J. Rodriguez, S.J. Marshall, G.W. Marshall, S.V. Kalinin, A. Gruverman, *J. Dent. Res.* **86**, 908 (2007)
145. V.R. Binetti, J.D. Schiffman, O.D. Leafner, J.E. Spanier, C.L. Schauer, *Integr. Biol.* **1**, 324 (2009)
146. M. Minary-Jolandan, M.-F. Yu, *Nanotechnology* **20**, 085706 (2009)
147. M. Minary-Jolandan, M.-F. Yu, *ACS Nano* **3**, 1859 (2009)
148. A. Gruverman, B.J. Rodriguez, S.V. Kalinin, in *Electromechanical Behavior in Biological Systems at the Nanoscale*, ed. by S.V. Kalinin, A. Gruverman. Scanning Probe Microscopy: Electrical and Electromechanical Phenomena on the Nanoscale, vol. 2, (Springer Science and Business Media, New York, 2007), pp. 615
149. C. Harnagea, M. Valléres, C.P. Pfeffer, D. Wu, B.R. Olsen, A. Pignolet, F. Légaré, A. Gruverman, *Biophys. J.* **98**, 3070 (2010)
150. S.V. Kalinin, S. Jesse, W. Liu, A.A. Balandin, *Appl. Phys. Lett.* **88**, 153902 (2006)
151. C. Harnagea, A. Pignolet, M. Alexe, D. Hesse, *IEEE Trans Ultrason, Ferroelectr, Freq Control* **53**, 2309 (2006)
152. B.J. Rodriguez, C. Callahan, S.V. Kalinin, R. Proksch, *Nanotechnology* **18**, 475504 (2007)
153. S. Jesse, S.V. Kalinin, R. Proksch, A. P. Baddorf, B.J. Rodriguez, *Nanotechnology* **18**, 435503 (2007)
154. B. Zeyen, K. Virwani, B. Pittenger, K.L. Turner, *Appl. Phys. Lett.* **94**, 103507 (2009)
155. S. Jesse, S.V. Kalinin, *Nanotechnology* **20**, 085714 (2009)
156. S. Jesse, P. Maksymovych, S.V. Kalinin, *Appl. Phys. Lett.* **93**, 112903 (2008)
157. J.N. Israelashvili, *Intermolecular and Surface Forces* (Academic, London, 1985)
158. M.E. Davis, J.A. McCammon, *Chem. Rev.* **90**, 509 (1990)
159. T.P. Hunt, R.M. Westervelt, *Biomed. Microdev.* **8**, 227 (2006)
160. A. Docoslis, L.A. Tercero Espinoza, B. Zhang, L.-L. Cheng, B.A. Israel, P. Alexandridis, N.L. Abbott, *Langmuir* **23**, 3840 (2007)
161. R.C. Hayward, D.A. Saville, I.A. Aksay, *Nature* **404**, 56 (2000)
162. K. Hu, A.J. Bard, *Langmuir* **13**, 5418 (1997)
163. H.-J. Butt, *Biophys. J.* **60**, 1438 (1991)
164. T.J. Smith, K.J. Stevenson, in *Electrochemical SPM: Fundamentals and Applications*, ed. by S.V. Kalinin, A. Gruverman. Scanning Probe Microscopy: Electrical and Electromechanical Phenomena on the Nanoscale, vol. 1 (Springer Science and Business Media, New York, 2007) pp. 280–314
165. C.A.J. Putman, K.O. Van der Werf, B.G. De Grooth, N.F. Van Hulst, J. Greve, *Appl. Phys. Lett.* **64**, 2454 (1994)
166. H.-J. Butt, *Biophys. J.* **60**, 777 (1991)
167. H.-J. Butt, *Biophys. J.* **60**, 1438 (1991)
168. V.G. Levandy, M.L. Belaya, D.A. Pink, M.H. Jericho, *Biophys. J.* **70**, 1745 (1996)

169. D.J. Müller, D. Fotiadis, S. Scheuring, S.A. Müller, A. Engel, *Biophys. J.* **76**, 1101 (1999)
170. A. Philippsen, W. Im, A. Engel, T. Schirmer, B. Roux, D.J. Müller, *Biophys. J.* **82**, 1667 (2002)
171. J. Sotres, A.M. Baró, *Appl. Phys. Lett.* **93**, 103903 (2008)
172. A. Noy, D.V. Vezenov, C.M. Lieber, *Annu. Rev. Mater. Sci.* **27**, 381 (1997)
173. J. Seog, D. Dean, A.H.K. Plaas, S. Wong-Palms, A.J. Grodzinsky, C. Ortiz, *Macromolecules* **35**, 5601 (2002)
174. A.S. Johnson, C.L. Nehl, M.G. Mason, J.H. Hafner, *Langmuir* **19**, 10007 (2003)
175. Y. Yang, K.M. Mayer, J.H. Hafner, *Biophys. J.* **92**, 1966 (2007)
176. Y. Yang, K.M. Mayer, N.S. Wickremasinghe, J.H. Hafner, *Biophys. J.* **95**, 5193 (2008)
177. D.J. Müller, A. Engel, *J. Mol. Biol.* **285**, 1347 (1999)
178. B.J. Rodriguez, S. Jesse, A.P. Baddorf, S.-H. Kim, S.V. Kalinin, *Phys. Rev. Lett.* **98**, 247603 (2007)
179. P.L.T.M. Frederix, M. R. Gullo, T. Akiyama, A. Tonin, N. F. de Rooij, U. Stauffer, A. Engel, *Nanotechnology* **16**, 997 (2005)
180. Y. Hirata, F. Mizutani, H. Yokoyama, *Surf. Interface Anal.* **27**, 317 (1999)
181. B.P. Lynch, A.M. Hilton, C.H. Doerge, G.J. Simpson, *Langmuir* **21**, 1436 (2005)
182. S.V. Kalinin, D.A. Bonnell, *Appl. Phys. Lett.* **78**, 1306 (2001)
183. S.V. Kalinin, D.A. Bonnell, *J. Appl. Phys.* **91**, 832 (2002)
184. P.K. Hansma, B. Drake, O. Marti, S.A. Gould, C.B. Prater, *Science* **243**, 641 (1989)
185. M. Böcker, B. Anczykowski, J. Wegener, T.E. Schäffer, *Nanotechnology* **18**, 145505 (2007)
186. P. Novak, C. Li, A.I. Shevchuk, R. Stepanyan, M. Caldwell, S. Hughes, T.G. Smart, J. Gorelik, V.P. Ostanin, M.J. Lab, G.W.J. Moss, G.I. Frolenkov, D. Klenerman, Y.E. Korchev, *Nat. Meth.* **6**, 279 (2009)
187. www.veeco.com/pdfs/datasheets/DS57-SECPM_04153_189.pdf
188. W.R. Bowen, A.N. Filippov, A.O. Sharif, V.M. Starov, *Adv. Colloid. Interface Sci.* **81**, 35 (1999)
189. S.V. Kalinin, B.J. Rodriguez, S. Jesse, K. Seal, R. Proksch, S. Hohlbauch, I. Revenko, G.L. Thompson, A.A. Vertegel, *Nanotechnology* **18**, 424020 (2007)
190. M.P. Nikiforov, V.V. Reukov, G.L. Thompson, A.A. Vertegel, S. Guo, S.V. Kalinin, S. Jesse, *Nanotechnology* **20**, 405708 (2009)
191. M.P. Nikiforov, G.L. Thompson, V.V. Reukov, S. Jesse, S. Guo, B.J. Rodriguez, K. Seal, A.A. Vertegel, S.V. Kalinin, *ACS Nano* **4**, 689 (2010)
192. R. Proksch, *Appl. Phys. Lett.* **89**, 113121 (2006)
193. T.R. Rodríguez, R. García, *Appl. Phys. Lett.* **84**, 449 (2004)
194. B.J. Rodriguez, S. Jesse, S. Habelitz, R. Proksch, S.V. Kalinin, *Nanotechnology* **20**, 195701 (2009)
195. R. Plonsey, R.C. Barr, *Bioelectricity: A Quantitative Approach* (Plenum Press, New York, 1988)
196. B.T. Rosner, D.W. van der Weide, *Rev. Sci. Instrum.* **73**, 2505 (2002)
197. B.J. Rodriguez, S. Jesse, K. Seal, A.P. Baddorf, S.V. Kalinin, P. Rack, *Appl. Phys. Lett.* **91**, 093130 (2007)
198. T. Fukuma, S.P. Jarvis, *Rev. Sci. Instrum.* **77**, 043701 (2006)
199. S.P. Jarvis, A. Oral, T.P. Weihs, J.B. Pethica, *Rev. Sci. Instrum.* **64**, 3515 (1993)
200. D.N. Richards, D.Y. Zemlyanov, R.M. Asrar, Y.Y. Chokshi, E.M. Cook, T.J. Hinton, Z. Lu, V.Q. Nguyen, N.K. Patel, J.R. Usher, S. Vaidyanathan, D.A. Yeung, A. Ivanisevic, *J. Phys. Chem. C* **114**, 15486 (2010)
201. B. Moores, F. Hane, L. Eng, Z. Leonenko, *Ultramicroscopy* **110**, 708 (2010)
202. D.M. Czajkowsky, M.J. Allen, V. Elings, Z. Shao, *Ultramicroscopy* **74**, 1 (1998)
203. O. Takeuchi, Y. Ohrai, S. Yoshido, H. Shigekawa, *Jap. J. Appl. Phys.* **46**, 5626 (2007)
204. N. Kobayashi, H. Asakawa, T. Fukuma, *Rev. Sci. Instrum.* **81**, 123705 (2010)